SANDIA REPORT

SAND2009-7168
Unlimited Release
Printed October 2009

Quantitative Study of Rectangular Waveguide Behavior in the THz

Michael Wanke, Adam Rowen, Chris Nordquist

Prepared by
Sandia National Laboratories
Albuquerque, New Mexico 87185 and Livermore, California 94550

Sandia is a multiprogram laboratory operated by Sandia Corporation,
a Lockheed Martin Company, for the United States Department of Energy's
National Nuclear Security Administration under Contract DE-AC04-94-AL85000.

Sandia National Laboratories

Issued by Sandia National Laboratories, operated for the United States Department of Energy by Sandia Corporation.

Available to DOE and DOE contractors from
U.S. Department of Energy
Office of Scientific and Technical Information
P.O. Box 62
Oak Ridge, TN 37831

Telephone: (865) 576-8401
Facsimile: (865) 576-5728
E-Mail: reports@adonis.osti.gov
Online ordering: http://www.osti.gov/bridge

Available to the public from
U.S. Department of Commerce
National Technical Information Service
5285 Port Royal Rd
Springfield, VA 22161

Telephone: (800) 553-6847
Facsimile: (703) 605-6900
E-Mail: orders@ntis.fedworld.gov
Online ordering: http://www.ntis.gov/help/ordermethods.asp?loc=7-4-0#online

SAND2009-7168
Unlimited Release
Printed October 2009

Quantitative Study of Rectangular Waveguide Behavior in the THz

Michael Wanke, Adam Rowen
Photonic Microsystems Technology

Chris Nordquist
RF/Optoelectronics

Sandia National Laboratories
P.O. Box 5800
Albuquerque, New Mexico, 87185

Abstract

This report describes our efforts to quantify the behavior of micro-fabricated THz rectangular waveguides on a configurable, robust semiconductor-based platform. These waveguides are an enabling technology for coupling THz radiation directly from or to lasers, mixers, detectors, antennas, and other devices. Traditional waveguides fabricated on semiconductor platforms such as dielectric guides in the infrared or co-planar waveguides in the microwave regions, suffer high absorption and radiative losses in the THz. The former leads to very short propagation lengths, while the latter will lead to unwanted radiation modes and/or crosstalk in integrated devices. This project exploited the initial developments of THz micro-machined rectangular waveguides developed under the THz Grand Challenge Program, but instead of focusing on THz transceiver integration, this project focussed on exploring the propagation loss and far-field radiation patterns of the waveguides.

During the 9 month duration of this project we were able to reproduce the waveguide loss per unit of length in the waveguides and started to explore how the loss depended on wavelength. We also explored the far-field beampatterns emitted by H-plane horn antennas attached to the waveguides. In the process we learned that the method of measuring the beam patterns has a significant impact on what is actually measured, and this may have an effect on most of the beam patterns of THz that have been reported to date. The beampattern measurements improved significantly throughout the project, but more refinements of the measurement are required before a definitive determination of the beam-pattern can be made.

Acknowledgments

This project could not have been accomplished without the efforts and diverse talents of the many people who significantly contributed to this project:

Dan Allen
Christian Arrington
Melissa Cavaliere
Mike Cich
Chuck Fuller
Rusty Gillen
Albert Grine
Terry Hargett
Andrew Hollowell
Mark Lee
Chris Nordquist
John Reno
Adam Rowen
Eric Shaner
Paiboon Tangyunyong.

In addition, we would like to acknowledge the funding by the Sandia Labratory Directed Research and Development (LDRD) program.

Contents

Appendix

List of Figures

Nomenclature

ac alternating current

cw continuous wave

dc direct current

EFL Effective focal length

FIR Far-infrared

FTIR Fourier-transform infrared spectrometer.

FTS Fourier transform spectrometer

GaAs gallium arsenide

GC LDRD Grand Challenge LDRD

HEB Hot Electron Bolometer

LDRD Laboratory Directed Research and Development program.

L-I-V Plot of light(L) and voltage(V) versus current (I) - typically used for lasers.

LO Local oscillator

MBE Molecular Beam Epitaxy

MIR Mid-infrared

OAP Off-axis Paraboloid

QCL Quantum Cascade Laser

RWG Hollow rectangular metal waveguide

SEM Scanning electron microscope (image)

TDS Time-domain spectroscopy/spectrometer

THz Short for terahertz (frequency equal to 10^{12} Hz)

Chapter 1

Overview

This work arose out of the developments made in a previous program, namely the Terahertz Microelectronic Transceiver Grand Challenge LDRD. While that work needed rectangular THz waveguides, it was focused on making transceivers. Therefore, the waveguide development and characterization were focussed solely for the application. With the successful demonstration that we could make and integrate THz rectangular waveguides with active THz components, we needed to look more closely at the waveguides themselves. This project set out to quantify the behavior of rectangular waveguides initially created under the THz Grand Challenge LDRD. This goals were divided into four desired measurements.

1. Quantifying the propagation loss / length of micromachined waveguides at a design frequency. *During the grand challenge, most of our efforts regarding waveguides were directed at learning how to fabricate the waveguides. We measured waveguide transmission and observed promising initial results for waveguide loss, but were only able to measure a couple chips. Here we wanted to measure more waveguides to provide a statistically significant result.*

2. Measuring the loss / length of the waveguides as a function of frequency to provide feedback to the models. *Single frequency loss measurements are useful for guiding the integration of the waveguides with single frequency QCLs, but to be more generally useful, we need to know the full waveguide frequency dispersion. This means measuring the waveguides over very broad frequency ranges, preferably from below the waveguide cut-off to above the frequency where a second mode is allowed. This provides critical design knowledge about the waveguide properties and provides feedback that can be used to compare with our design models. These measurements may be particularly helpful in understanding the importance of the imaginary component of the metal complex conductivity, which is negligible and usually ignored at microwave frequencies but has to be accounted for in the THz.*

3. Measuring far-field beam pattern emitted by a micro-lithographically created rectangular horn. *Efficiently coupling a THz signal into or out of the rectangular waveguides is essential for most waveguide applications and providing a single spatial mode far-field pattern is essential for many heterodyne applications. The few beam pattern measurements made under the Grand Challenge showed qualitative agreement with models, but they displayed many unexpected features which needed to be resolved.*

4. Measuring beam pattern of a QCL coupled out through a horn antenna. *Since the rectangular waveguide should act as a mode filter and only allow TE10 to propagate (over a certain frequency range), this measurement should in principle give the same beampattern as in measurement 3. However, there is no real evidence supporting this conjecture yet and we do not yet know how long the waveguide would have to be in order to completely filter out other*

modes. The THz Grang Challenge also demonstrated that we could integrate a QCL into a waveguide and get the light out of the horn, but stress damage prevented acquiring the beam patterns and probably distorted the beam patterns as well. Therefore we worked on lowering thermally induced stress in the waveguides before trying to measure the beampatterns.

While prototype waveguides (both stand-alone and integrated with lasers) were demonstrated in the prior program, yield and reproducibility were still significant issues. So implicit in the above measurements was the requirements of improving the processes that created these structures as well.

The waveguide propagation loss both as a function of length as a function of frequency are discussed in chapter 2, the progress towards measuring the beampattern emitted by a micromachined horn antenna is discussed in chapter 3 and our efforts to improve integration of QCLs with rectangular waveguides and measure a beampattern emitted by the combined device are discussed in chapter 4.

Since the basic concepts of the waveguides as well as the motivations for developing them are well described in the final report for the previous project (see document SAND2008-7337), this report will be focussed on the measurements.

Chapter 2

Waveguide Loss Measurements

The measurements for determining the waveguide loss were conceptually the same as the waveguide loss measurements described in the THz GC LDRD SAND report. Enough of the description will be reiterated here so that the following can be understood in isolation, but further details can be found in the document SAND2008-7337. In this work, further refinements were made to the previous measurements and these will be described in detail here.

In the THz Grand Challenge, two sets of masks were created to explore the properties of stand-alone rectangular waveguides. All the work done this year used the second mask design. The full documentation regarding the design of these mask set is provided in App. B.1.2 in SAND2008-7337.

2.1 Sample Geometry

To extract the loss of the waveguides we used a series of waveguides with different lengths. These waveguides were created on silicon substrates as described above and divided into 80 mm x 4 mm rows containing 16 waveguides (see Fig. 2.1). Each waveguide is terminated with a waveguide horn on opposite sides of the bar for coupling THz radiation into and back out of the waveguides. These apertures are collinear to facilitate alignment of the optics used for coupling the THz radiation to the waveguides. The horns edge-emit from the long (100 mm) edge of the bar, and are spaced on 5 mm pitch. Of the 16 waveguides shown in Fig. 2.1, six waveguides are straight and nominally identical to each other. The length of these waveguides is 2.6 mm excluding the flared horns. The remaining 10 waveguides follow a meandering path, each with 24 corners, to achieve different lengths varying from 14.25 mm to 38.65 mm (excluding the horns) in 6 mm steps. These 10 waveguides are divided into two nominally identical sets of 5 WGs each (waveguides 4-8 and 10-14 respectively).

Figure 2.1. Composite image of 3 pictures of a single row of free space waveguides (sample 06-24-08-02 Row 9)

Scanning electron microscope images of two waveguides (2 and 7) are shown in Fig. 2.2. The waveguide path can be determined by the photoresist removal holes that are placed at regular intervals in the waveguide lid The different lengths of the meandering waveguides were obtained by changing only the length of the horizontal straight sections of the waveguide shown in Fig. 2.2(b). Since the horns and bends are identical on each of the waveguides, losses arising from the antenna

coupling and bends should be the same for each. Thus differences in the transmission between waveguides should relate only to the propagation loss along the waveguides.

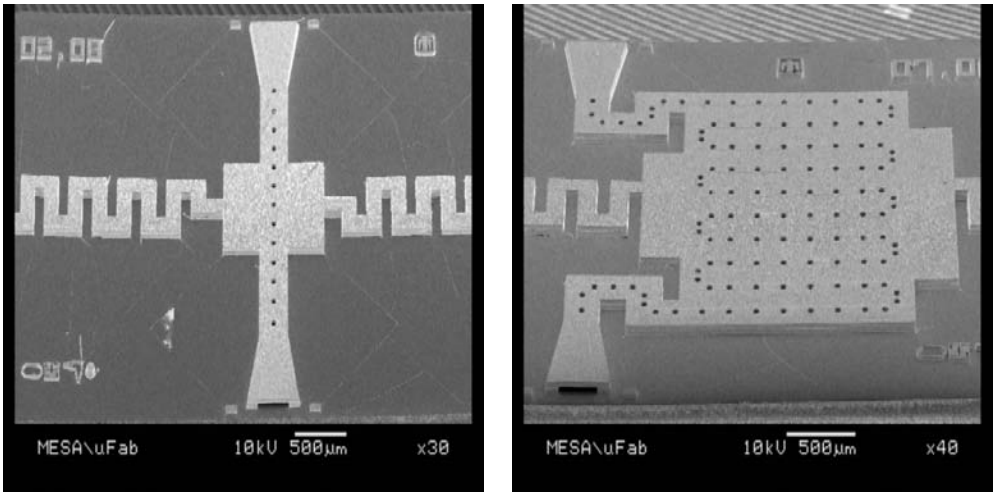

(a) **(b)**

Figure 2.2. SEMs of two free space coupled rectangular waveguides showing horns on both ends of the waveguides for coupling light in and out. The waveguide path follows the visible release holes. The horns are always directly across from each other on the chip with apertures typically 4 mm apart from each other. (a) A straight waveguide of length 2.6 mm. (b) A longer waveguide with 24 bends and length 20.25 mm. Lengths do not include the horns.

2.2 Sample Mount

To prevent light from leaking around the waveguides during measurements we mounted the samples into aluminum mounting jigs. The method of mounting the sample into the jigs is critical for obtaining good transmission results especially for the longer waveguides where any leakage can swamp the signal going through the waveguide.

A cartoon and a picture illustrating our initial approach for sample mounting is shown in Fig. 2.3. Indium foil was placed between the sample and aluminum pieces to guarantee a tight seal. Unfortunately, indium could flow into the release holes if excessive force was applied to the jigs while mounting the samples. Since the chip itself is almost atomically flat, while the pressing surfaces of the jigs are only smooth on the scale of one to two mils (25-50 microns), there were always places where more pressure was applied. This led to indium either squeezing through some of the release holes if the jig was tightened enough to eliminate all gaps or led to residual gaps above the waveguides that light could leak through if we ensured no indium squeezed into the holes. Another issues that caused non-uniform squeezing was the non-similar areas of raised gold around each waveguide as can clearly between the two waveguides shown in fig. 2.2. We observed that the indium would tend to compress around and into the straighter waveguides, while at the same time there was almost no compression of the indium over the longer meandering waveguides. The

former has more room for the indium to flow around the waveguides while the latter does not and therefore the indium above the latter is in a sense less "compressible". With only two screws at the ends of the aluminum jig is it not possible to apply more force to one area compared to another so this will always be a problem with these mounting jigs.

Another issue with using thin indium foil is that the foil is very soft and non-rigid which makes it difficult to stack all the elements and keep them aligned when mounting. Besides taking a lot of time, this was not a serious issue by itself. However, the jig itself is only a couple mm thick and does not cover all of the release holes. If the indium was not aligned well to cover these holes light could also couple in through these holes, and bypass some of the waveguide length. However, covering these holes was risky since if we touched up the indium by pressing it around openings, the relatively sharp tip used to manipulate the indium could easily push indium into the release holes. Because of the non-uniform indium compression, difficultly in mounting alignment and issues with the exposed holes on the chip we continued to seek alternative solutions.

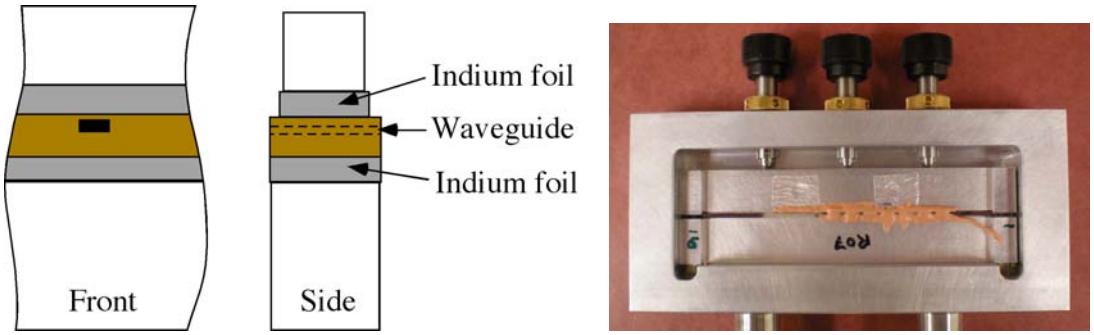

Figure 2.3. (a) Cartoon and (b)picture of a free-space rectangular waveguide strip mounted in measurement jig. Two pieces of indium foil are sandwiched between the jig and sample on both sides of the sample. To help compress the indium uniformly, the sample jig is placed in a measurement jig with screws along it's length. The orange substance on top of some of the waveguides is silly putty.

The next iteration we considered was to plate indium on both sides of a Si wafer and dice out strips 80 mm x 3.5 mm. These strips could then replace the indium foil (at least the foil on top of the waveguides). These provided a rigid carrier for the indium which made it much easier to align with the waveguide strips. Having straight strips exactly 3.5 mm wide along their entire length also made it possible to cover the release holes reliably. For the first samples the indium on the side pressing against the waveguides was kept to 10 micron thickness to minimize the chances of indium squeezing all the way through a release hole into a waveguide. The other side had 50 microns of indium to compensate for the non-planar jig surface. Unfortunately, when the screws of the jig were tightened, the indium compressed completely near the ends of the chip, while a gap opened between the chips near the center. Releasing the screw pressure reduced the gap size (but still not not make a light tight seal) and lifted the chip near the ends (resulting in a gap between the irreversibly compressed indium and the the tops of the waveguides near the edges. Trying another sample with the 50 micron thick indium layer in contact with the chip resulted in the same behavior

except that the indium squeezed all the way into the waveguides. Thus the Si wafer is rigid enough to allow alignment of the chips but it is not rigid enough to maintain planarity over its entire 80 mm length when compressed at the ends.

To minimize the chip bowing, we built a second measurement jig to hold the mounting jig. This measurement jig (shown in Fig. 2.3(b)) uses three differential micrometer screws along the length of the mounting jig to apply pressure more uniformly along the length of the sample instead of just at the ends. These screws had a differential mechanism that moved the tip of the screw as little as 25 microns per revolution which allowed compression of the indium in a much more controlled fashion. Since we determined that the silicon pieces were not rigid along their length when compressed we again inserted indium foil between the silicon pieces and the jig to smooth out some of the irregularites in the jig surfaces. This actually reduced a lot of the leakage that was observed. Unfortunately, if the differential screw pressure was released for any reason (e.g. to switch to another chip and then come back for remeasurement or to touch up the indium by hand) the chips would not remain remain compressed uniformly and gaps would reopen.

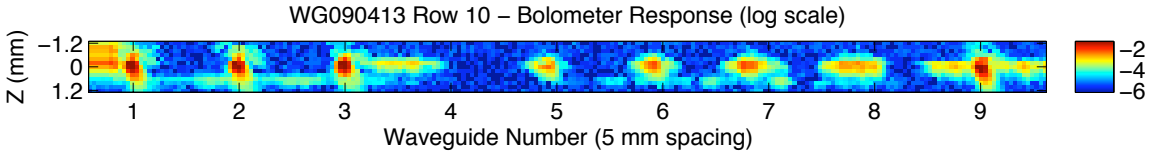

Figure 2.4. 2D image of the transmission through sample 090413 Row 10 captured by scanning the waveguide chip through a THz beam. The waveguides should reside at z=0 and directly above the numbers on the x-axis. The bottom of the waveguide substrate is near z = 0.6 mm. Leakage of light at both the top and bottom interfaces is clearly visible.

Even with the first uniform compression there was still some leakage. Fig. 2.4 gives an example 2D transmission image that shows two major areas of leakage. One area is along the line corresponding to the interface between the aluminum jig and the bottom of the substrate holding the waveguides (z = 0.6 mm in the image), and the other is in the plane of the waveguides (near z = 0). The leakage for z = 0 occurs in areas between large meander lines. The light transmission near waveguides 5,6,7 and 8 is to the left of waveguide and the width of the leakage corresponds roughly to the separation between the meander lines (which can be seen in fig. 2.1). Thus it appears that we have compression difficulties of the indium near the big meander lines which prevents pressing the indium down between the lines where there is very little material and hence more chance of light leaking through. In order to fill these gaps and also to minimize leakage when the pressure on the chip was released we applied silver paste. This should be rather opaque to THz radiation. However, we found that the paste did not reduce leakage (at least with the film thicknesses we used).

We did note, however, that we were able to patch the big light leaks at the very end of the chips. To provide something for the silver paste to sit on while it dried we had inserted silly putty into these openings. After we saw leakage through the silver paste around the waveguides but not at the ends where the silver paste was on top of the silly putty, we wondered if silly putty would be a better THz absorber. Therefore we put silly putty on the top and bottom of the chip to fill

in any perceived gaps. This reduced the leakage significantly but still left some leakage right at the top and bottom surface of the chip. This suggested that some of the light is actually leaking through sputtered gold on the substrate facet allowing light to travel through the substrate. Given the roughness of the facet surface and the sharp corner at the top and bottom surfaces it is possible that there are microcracks at the sharp corners allowing light to propagate through the substrate. Therefore we covered the whole face of the chip (except for small holes around the waveguide openings with silly putty. After this the leakage was essentially zero. Besides actually working as a strong THz absorber, silly putty has the advantage that it can easily be removed and reapplied as required, and it does not permanently glue the chips together like the silver paste does.

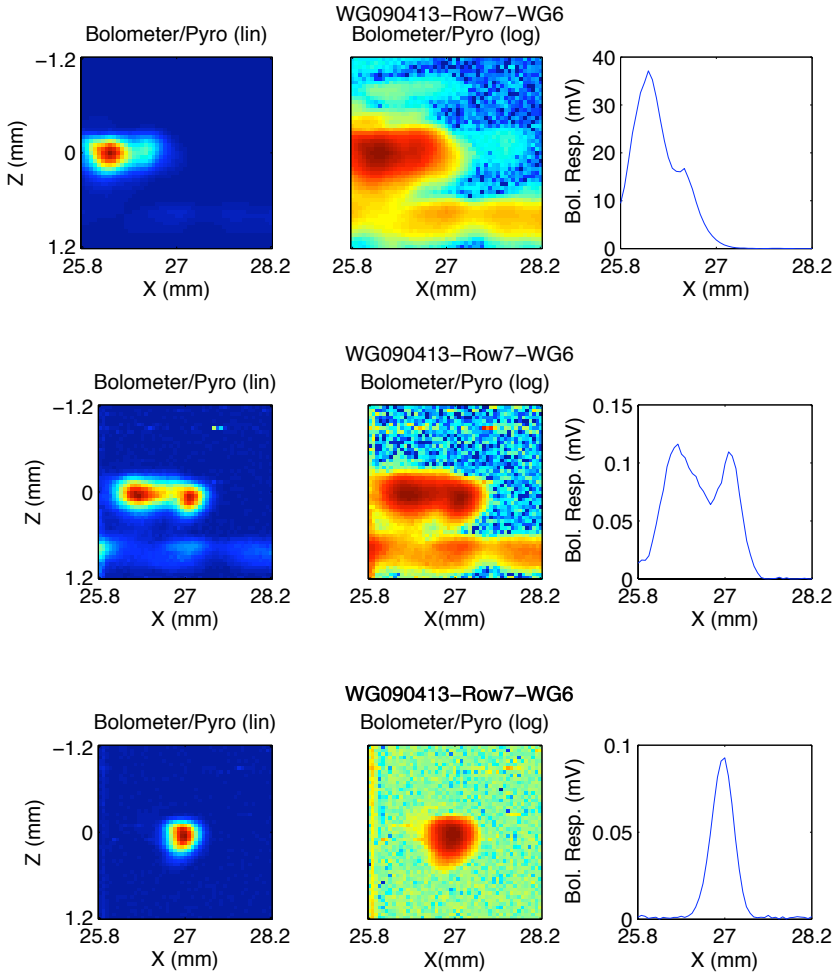

Figure 2.5. Three consecutive measurements of the transmission of sample 090413R7WG6 with different levels of leakage mitigation efforts. The top only has silver paste added, the middle has silly putty above applied to the interfaces of the waveguide chip on one side and the bottom has silly putty on both side of the wafer covering everything (including the substrate facet) except for a small area around the waveguide opening.

Fig. 2.5 shows 3 transmission images for a single waveguide taken over 2 days. The first used silver paste only, the second has silly putty on one side of the waveguides, above and below the chip, and the third has silly putty on both side with the putty covering the facet of the substrate except where the around the waveguide.In the first the leakage next to the waveguide is so strong that it overwhelms the waveguide transmission which appears only as a little kink in the transmission. In the second leakage is still present and the waveguide transmission is riding on the side of a leakage peak of similar magnitude, but the actual transmission can be approximately extracted. In the third, the waveguide leakage is removed and the waveguide transmission is easily determined.

2.3 Measurement Set-up

The waveguides are characterized using a molecular gas far-infrared laser source (FIRL). This source of radiation is capable of generating radiation at a set of distinct lines by pumping select gasses with a CO_2 laser, with output powers up to a few 10's of mW's dependening on the frequency of operation.

The experimental set-up is shown in Fig. 2.6. THz radiation is generated by the FIRL. Part of this radiation is picked-off by a beamsplitter and sent to a pyroelectric detector that monitors the laser power. This signal is used by the FIRL controller to keep the power roughly constant, and is recorded during the measurements to correct for the remaining laser power fluctuations when we are measuring transmission through the waveguides. The pyroelectric element is tilted with respect to the incoming beam direction to prevent reflected light from returning to the laser which can effect laser stability. The rest of the radiation is sent to the row of waveguides being

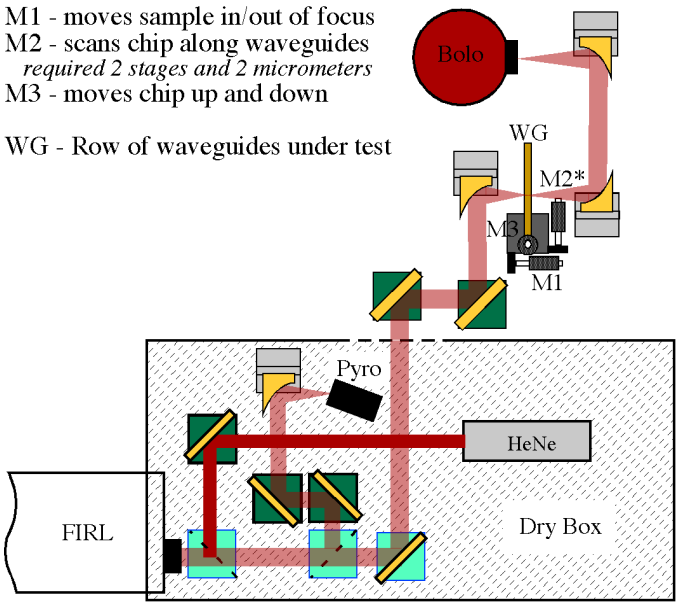

Figure 2.6. Optical set-up for the empty waveguide propagation measurements.

tested (denoted by WG in the figure). An off-axis paraboloid focusses the radiation to a spot

in the plane of the waveguide apertures. Light transmitted through a waveguide is collected on the other side by another off-axis paraboloid (OAP) and directed to a silicon bolometer detector. The waveguides being tested are mounted on a 3-axis translation stage. The two axes controlling motion perpendicular to the beam direction are motorized so that we can scan the entire chip to test where light comes through the waveguides or leaks through undesired paths. The third axis was set manually so that the waveguide openings were in the focal plane of the mirror.

To determine the propagation loss inside the waveguides, we compared the relative transmission through waveguides of different lengths. Doing this it is essential that the input to each waveguide be identical. Therefore the chip was aligned very carefully so that as it was scanned perpendicular to the beam path that it always remained in the focus of the off-axis mirrors. If the chip moved out of the focal plane the beam spot would have increased in size and the effective power coupling into the horn would drop. (see Fig. 2.7). We could double check our alignment (as well as the focal spot size and shape), by looking at the transmission as a function of position as the waveguides were scanned through the beam spot and comparing the images from different waveguides. In this regard, the straight waveguides that were nominally identical and were found at both ends and the middle of the chip were quite useful. While care was taken in this regard, there still may be some variation present in the collected data. Another issue that could effect the relative transmission

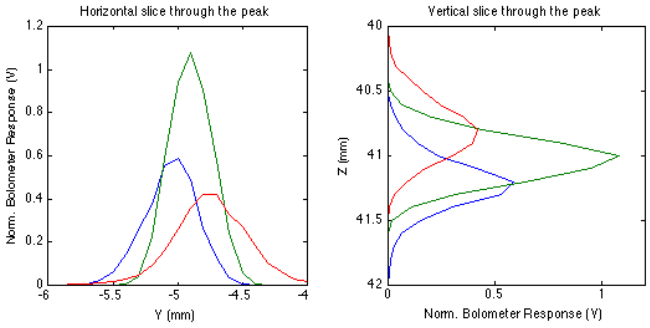

Figure 2.7. Cross-sections through the peak in 2D scans of transmission though a pinhole at (green), in front of (blue) or behind (red) the focal plane of the focussing off-axis paraboloid.

between waveguides was feedback of THz radiation reflected back from the waveguide chip into the FIRL. This can lead to two effects: (1) modulation the output power of the FIRL and (2) alteration the output spatial mode of the FIRL. The first can be corrected for by normalizing the response with the instantaneous power read by the pyroelectric reference detector, but the second leads to a different distribution of the energy in the focal-plane and is not something that can corrected.

Figs. 2.8, 2.9 and 2.10 show some of the feedback effects that we observed. The first figures two show periodic features in the pyroelectric response that reflect very small tilts of the waveguides (each fringe corresponds to roughly $1/2\ \lambda = 50\ \mu$m) change in the sample position along the beam propagation direction. These typically just indicated power fluctuations of the laser and were easy to take into account. Fig. 2.10 shows an instance when there was very strong feedback which huge effects on the laser power. Here the power drop was most likely caused by the second effect and could not be corrected.

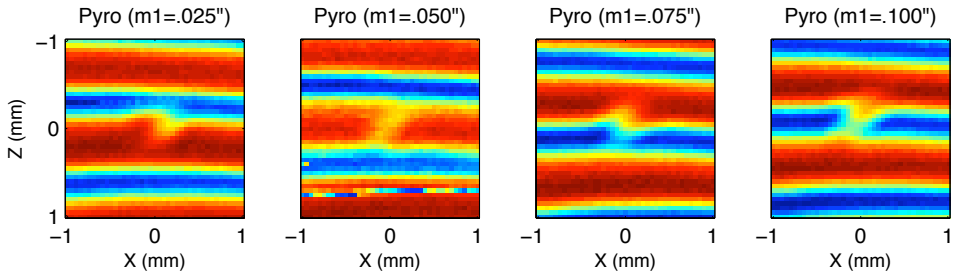

Figure 2.8. The response of the pyroelectric reference detector as a function of a 400 micron pinhole position near the focus of FIRL laser. Dark red corresponds to 1.5 times the intensity as the dark blue. Each 2D image corresponds to the pinhole being scanned perpendicular to the beam propagation over a 2 x 2 mm area, while the difference between images corresponds to the pinhole being moved along the beam propagation in roughly 64 micron steps. The intensity fluctuations depend on the effective length of the cavity compared to integral numbers of wavelengths between the laser and the reflecting surface of the pinhole. This length changes as the pinhole is scanned laterally due to $\approx 3^\circ$ of the pinhole holder.

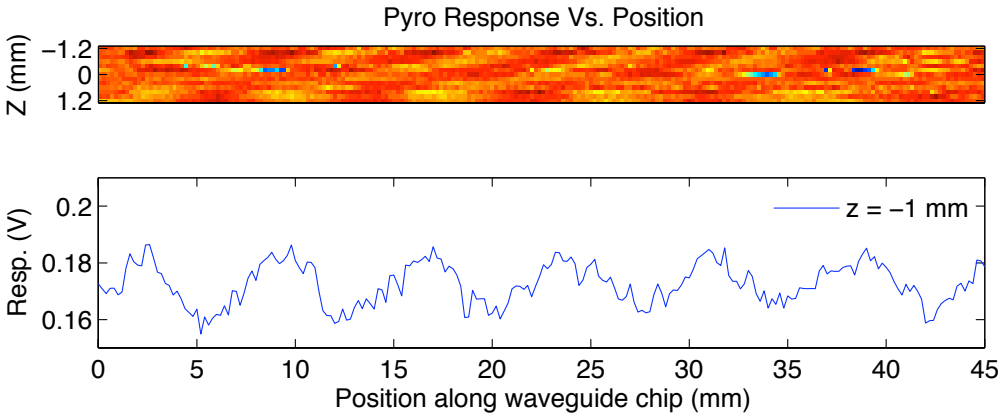

Figure 2.9. The response of the pyroelectric detector as a function of the position of the waveguide array. The top image shows the 2D transmission image while the bottom is a slice at $z = -1$ mm. The fringes suggest that the waveguide is tilted from end to end by ≈ 300 μm, and tilted top to bottom by ≈ 75 μm. In this case, the end to end deviation is too large compared to the allowable variation to allow quantitative comparisons between transmission measurements of different waveguides.

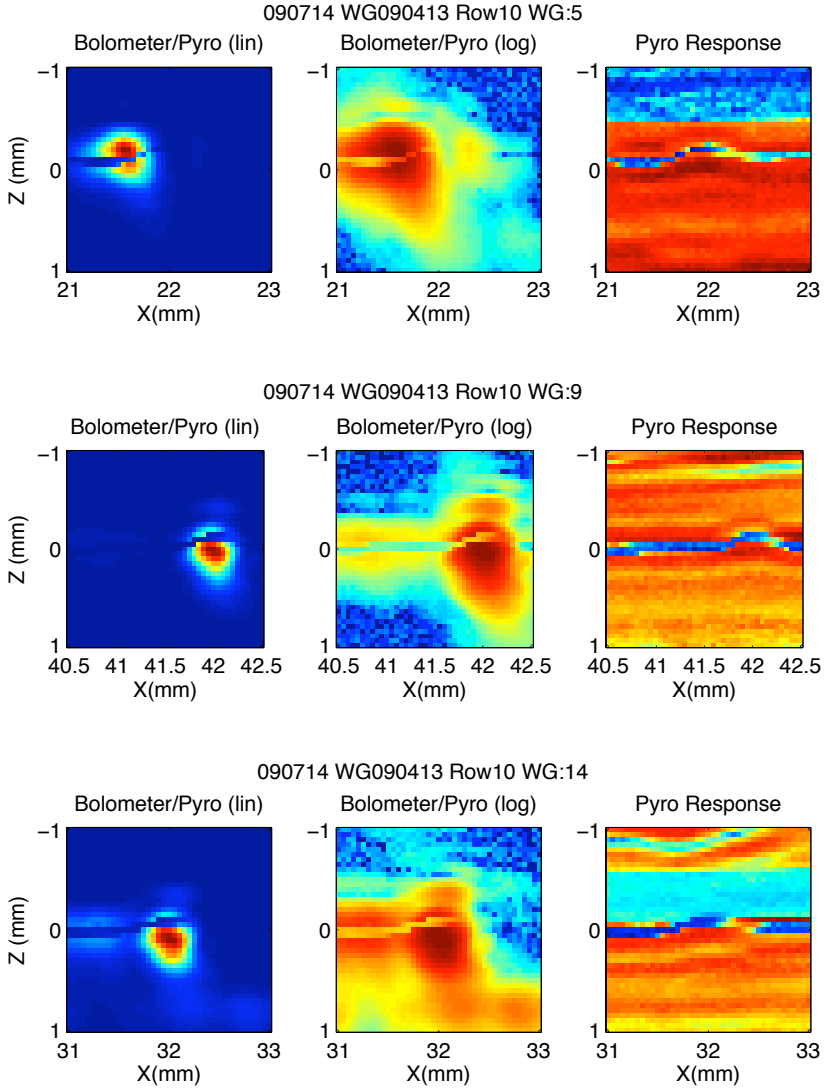

Figure 2.10. Transmission measurements of three waveguides on sample 090413R10 showing laser power drop out when the beam is focussed onto the interface between the chip and the jig. The larger block like changes in the laser power are normal fluctuations of the laser and are easily normalized out, but the drop at the interface leads to holes in the data on the left. The waveguides positions at 22, 42, and 32 mm are observed as a bump in the low power line seen in the pyro data.

To minimize the feedback effects, we took advantage of the fact that the beam diameter of the FIRL beam was less than half the diameter of the off-axis paraboloid. Instead of centering the input beam onto the OAP we lowered the input beam by 1 inch (see Fig. 2.11(a)). The light reflected off the mirror still focussed onto the waveguide opening, but now all the rays of light within the cone of focussing radiation propagated upward somewhat. Since most of the sample mount had vertical surfaces (the aluminum jig, the waveguide facet, etc...) most of the reflected radiation continued to propagate upwards and therefore hit the upper side of the OAP. In this way the reflected radiation did not overlap the incident beam spatially and therefore it did not couple back into the FIRL. This removed the fringe pattern normally seen on the reference detector, but because the chip jutted out of the aluminum jig a little distance, when the beam was focussed right at the intersection between the two the light could retro-reflect as depicted in fig. 2.11(b). The consequences of this on the laser power is seen in fig. 2.10. Fortunately both the silver paste and silly putty seemed to remove this remaining retroreflection.

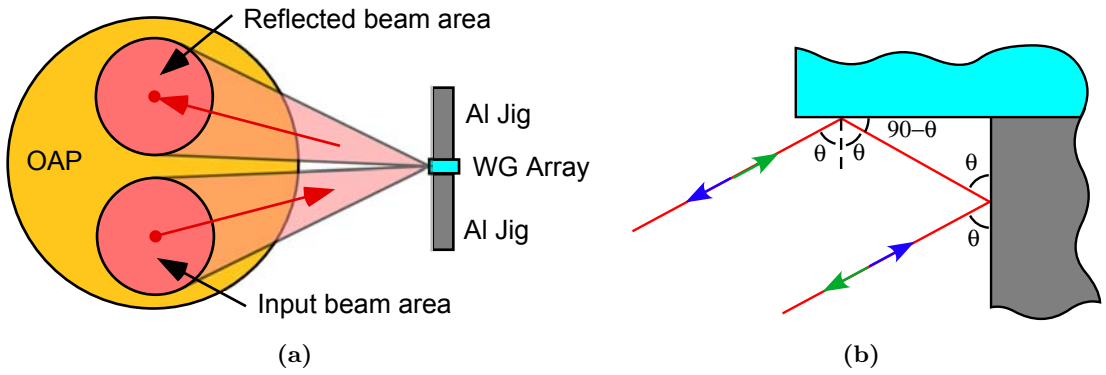

Figure 2.11. Cartoon depicting the optics positioning used to minimize retroreflection of THz radiation reflecting off of the measuerment jig back into the laser. (a)The input beam was lowered and only reflected off of the lower half of the off-axis paraboloid resulting in a rising beam. The reflected beam hit the upper part of the OAP so that the two beams were spatially separated. (b) Only when the input beam was focussed near the intersection of the jig and sample could the beam retroreflect back into the FIRL.

Besides significantly reducing feedback this had two other important consequences. The first was that this actually should have improved the coupling into the waveguides since the computed far-field patterns of the horn antennas predicted an optimal angle that was not along the boresite of the waveguides but was tilted up off the surface of the chip by roughly 30°.With the offsets we used the central ray should have a rising angle of $\approx 25°$. Since we mounted the chips upside down this rising beam was closely matched the beampattern of the horn. The second consequence was that the beam shape was distorted compared to the input beam. Since we rarely achieved a really good gaussian beam shape from the FIRL, this probably was not significant, but it generally it should reduce the coupling to the waveguides. Since the coupling should be the same for each waveguide, both of these effects should really only make a difference in the overall signal to noise we get on the bolometer and should not effect the relative transmission between different waveguides.

2.4 Waveguide Loss - Results

As mentioned above, to obtain the loss per length for the waveguides we compared the transmission through waveguides of different lengths. Since the transmission will depend on the alignment of the input beam to the waveguide aperture, we captured the 2D image of input beam by scanning the waveguide through the focal point. The effective transmission for each waveguide was either taken as the peak transmission value in the 2D image, or as an average of the transmission over a finite number of pixels around the peak. Both methods gave nearly identical results.

Fig. 2.13 shows the transmission images for 5 waveguides ranging in length from 14.25 mm to 38.65 mm. In the images, red corresponds to the maximum intensity and blue the weakest intensity for that given figure. Therefore the colors cannot be compared between images. A few things can be noted by looking at these images. In the linear scale, the transmission image(as noted by the bolometer response) appears to be a fairly featureless spot. The middle images (on a log scale so that weaker intensities can be seen) shows much more intensity variation over the 2D area. We can tell that this is actually due to the input beam shape because the same pattern appears in each waveguide. Thus these patterns are not leakage as we saw above. As the waveguides get longer, the signal to noise drops and the pattern becomes harder to see.

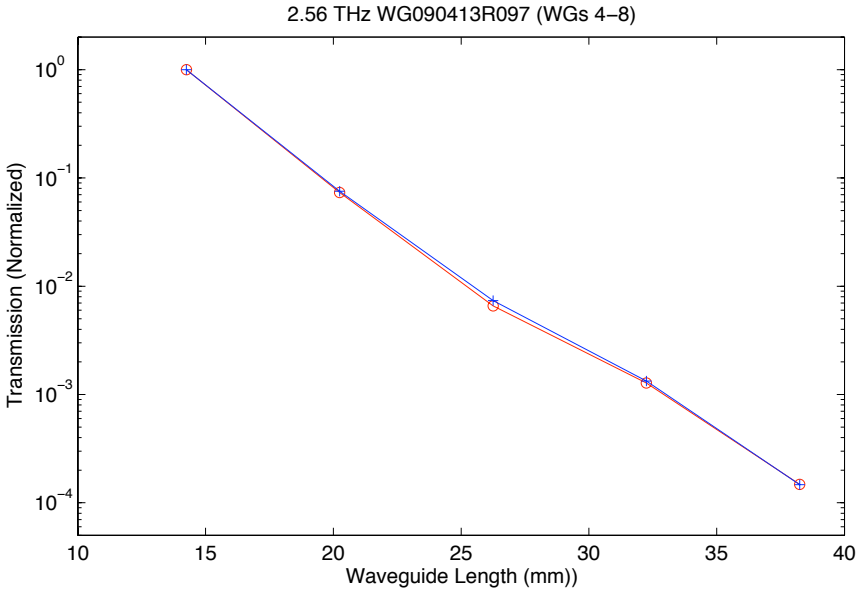

Figure 2.12. Relative transmission for different length waveguides. Each waveguide is normalized against waveguide 8.

The transmission for each waveguide normalized against the transmission of the shortest waveguide with an input frequency of 2.56 THz is shown in Fig. 2.12. By extracting the slope of this line, we can calculate the loss per length. I suspect that the slightly higher values seen in the longest two waveguides is due in part to the noise in the measurement. In fact in most of the measurements on various waveguides, the data for the longest two waveguides show a lot of fluctuation. Therefore, these waveguides were not included when determining the loss per length.

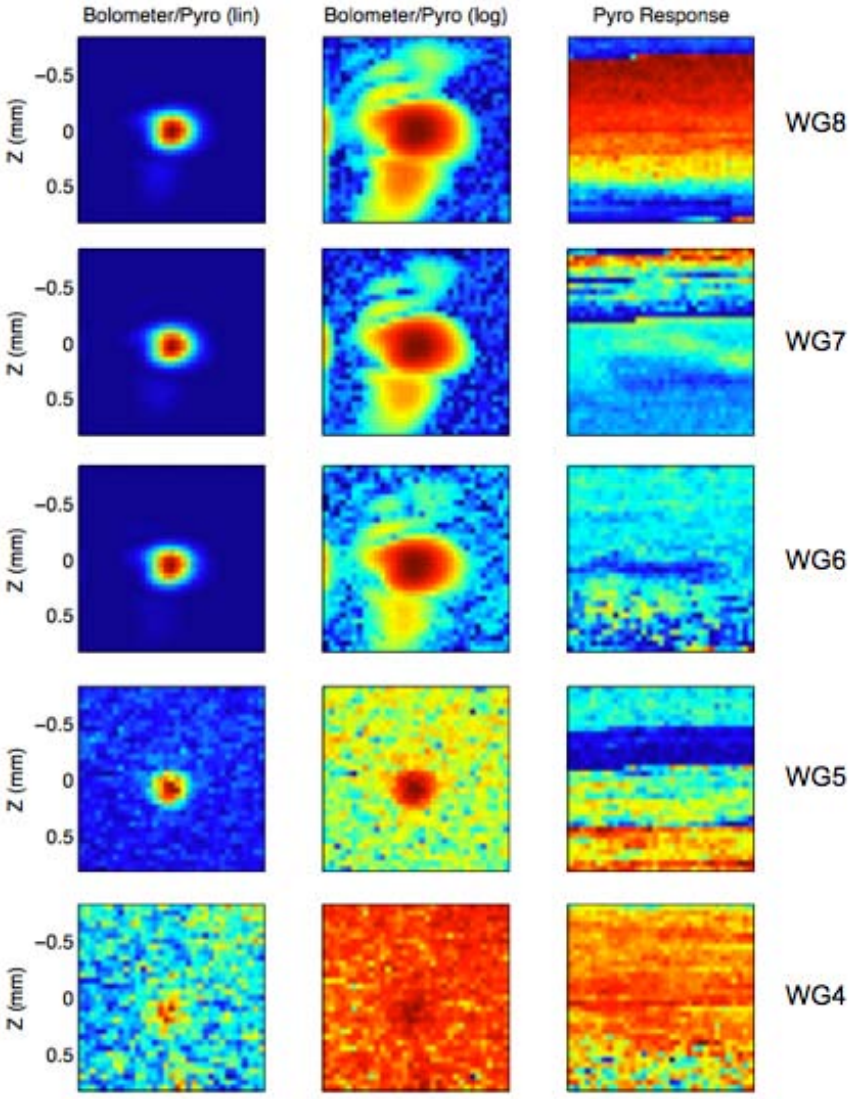

Figure 2.13. 2D Transmission images through a set of different length waveguides. The left column in the standard image, the middle is the same image with the intensity scaled by the log so that more dynamic range is available for illuminating more detail of the beam shape, and the right column shows the intensity fluctuation of the laser. The similarities between the patterns seen for different waveguides indicates that the coupling of the beam to the waveguides is fairly consistent.

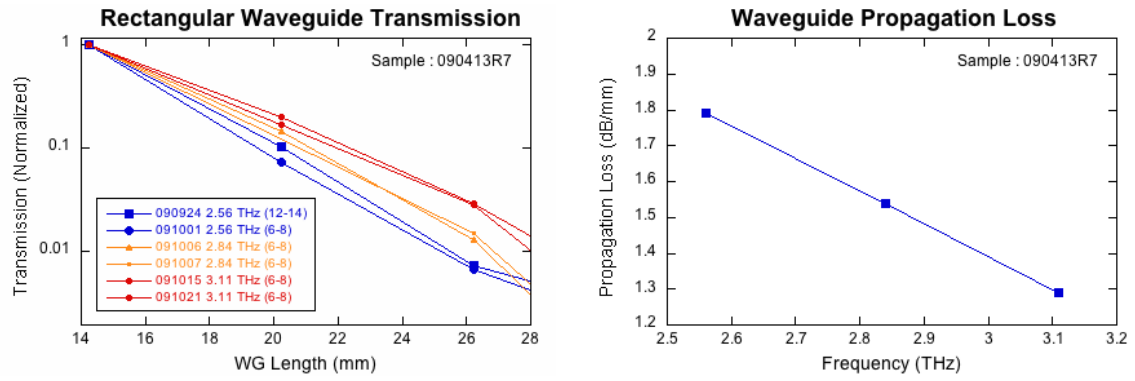

(a) **(b)**

Figure 2.14. (a) The transmission as a function of waveguide length and laser frequency. (b) The loss per length as a function of frequency as extracted from (a).

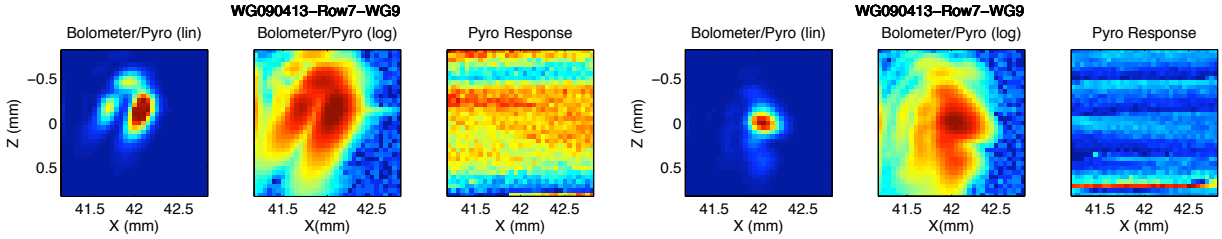

(a) **(b)**

Figure 2.15. The spatial pattern of the FIRL focal spot used for the (a) first transmission meausrements at 3.1 THz and (b) the second set of transmission measurements at 3.1 THz.

The transmission for two sets of waveguides at 2.56 THz (blue curves), and for multiple frequencies in one of the sets of waveguides is shown in Fig. 2.14(a). We can see that the two sets of data at 2.56 THz are fairly consistent with each other even though the measurements below to different waveguides. We can also see that as the frequency increases the slope becomes less negative which means that the loss decreases. This is what one expects for rectangular waveguides. The two curves taken at 2.84 THz (orange) were taken on different days but with everything else the same, while the two curves at 3.11 THz (red) were taken with the FIRL running on different spatial output modes between the two measurements (see fig. 2.15). Both of these sets of data appear to reproducible suggesting that as long as the data are normalized with respect to waveguide 8, the results for the loss per length appear to be the same.

It should be pointed out that when we changed the mode shape, the bolometer versus pyro signal changed a lot, so if the FIRL spatial mode changed during a measurement the data could not be used. This was another reason why imaging the transmission was useful.

Chapter 3

Stand-Alone Beampattern Measurements

When measuring quantum cascade laser beampatterns, the beam pattern looks smooth until you measure it with an angular accuracy on the order of 1° or better. This variation on a scale smaller than 1° is very unexpected and its cause is not fully understood. However, since one of the goals of this work is to demonstrate that integrated rectangular waveguide horns can improve the far-field pattern of QCLs, we need to be able to measure beampatterns to better than 1° accuracy.

One consequence of this requirement is that we will need a fairly sensitive detector. The output of the FIRL laser is typically only a few mW. Due to the large mismatch in the sizes of the beam-spot focussed onto the waveguide horn and the horn aperture, the power emitted by the horn is typically only microwatts. A 1° area corresponds to roughly 0.0004 steradians. Since the area of a halfsphere that the radiation can expand into is 2π steradians, if the power spread uniformly the power in each 'pixel' would be 6×10^{-6} the total power emitted. This lowers the microwatt of power transmitted to the order of picowatts. Fortunately, the power will not spread out uniformly, and should be concentrated over a smaller area, but to measure the beampatterns accurately, we want to use a cryogenically cooled silicon bolometer.

3.1 (Overly) Simple Beampattern Measurement

For our early attempts to measure the beampattern, we placed a pinhole between the waveguide and the first collection OAP (see Fig. 3.1). Throughout the measurement the laser, waveguide, optics and bolometer remain stationary, while the pinhole is scanned over a 24 mm x 24 mm area. The advantages of this approach include (a) only having to move a small pinhole over a small area and (b) keeping the coupling between the FIRL and WG constant. Disadvantages include the facts that (a) the effective steradian area of the pinhole changes as the pinhole moves further off the axis of the waveguide, (b) the measured 2D pattern has to be mathematically converted to get the angular emission pattern, (c) the accuracy of the conversion depends on the alignment of the mirrors, (d) the coupling of the light into the bolometer will change for different rays due to the angular dependence of the Fresnel reflection off the bolometer windows and (e) as we will see below interference effects.

The beam pattern for a typical horn is shown in Fig. 3.2, with the FIRL frequency set to 2.56 THz, the pinhole diameter equal to 400 μm, and a pinhole translation step size of 200 μm. As expected there does appear to be more divergence in the vertical direction than the horizontal

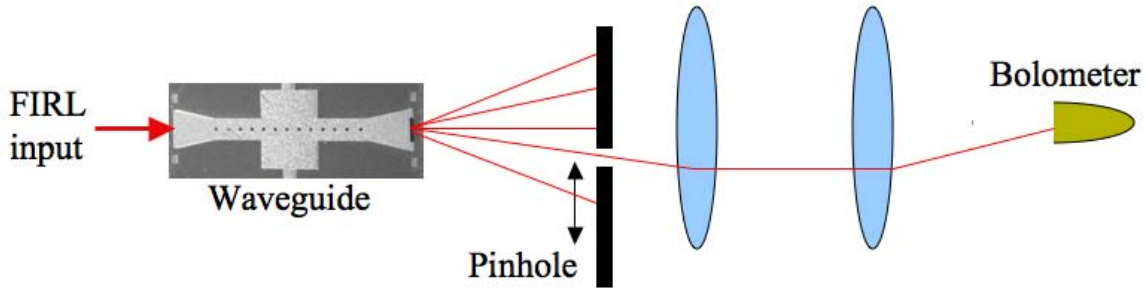

Figure 3.1. Schematic of measurement method for extracting the beam-pattern. Radiation from a FIRL laser is focussed into one end of a waveguide. The radiation propagates through the waveguides and diverges from the horn antenna on the opposite side. A pinhole allows only a specified angle of the emitted beam to be collected and and refocussed onto the detector. The actual lenses consist of two off-axis front surface reflective paraboloids (so there should not be any backreflections from them).

direction, although the difference is not as dramatic as expected. Much more unexpected, is the appearance of very fast oscillations which were not predicted in the models and doesnt make intuitive sense for a sub-wavelength aperture. The oscillations swing wildly even on the single pixel scale which is only a few wavelengths across. As we will show in the next few pages, this is caused by multi-beam reflection interference between the pinhole and the waveguides.

3.1.1 Interference Effects

We did not believe that these high-spatial-frequency oscillations in the beam-pattern could be created by the horn. Therefore we suspected some kind of multi-beam interference resulting from reflections between the waveguide and the detector. (Between the laser and the waveguide was ignored since there is nothing moving on that side of the waveguide and the single mode nature of the waveguide should filter out any interference patterns on the input). Theoretically there are only two optical elements between the waveguide and detecting element that should result in any backward propagating beam: the pinhole and the bolometer window. Thus the three possible cavities that we needed to explore were between: (a) the waveguide and the pinhole, (b) the waveguide and the bolometer, or (c) the pinhole and the bolometer. The laser frequency is 2.56 THz giving a wavelength of 117.1 μm. For every 25 μm displacement of an element, the path length of interfering beams should change by 50 μm or 0.427λ. This should alter the phase of the pattern noticeably. Therefore, to test for interference in these cavities we changed their path length controllably and looked for changes in the fringe pattern.

Unfortunately, the pinhole was not on a translation stage on the one axis we would need to change the effective cavity length with other elements, so we left it alone. Instead for the first measurement we moved the waveguides by 0.001" increments (one tick on the micrometer labelled M1). Since this is the resolution of the micrometer the exact change is not precisely known, but it should be roughly 25 μm which is a little less than $1/4\lambda = 29.27; \mu$m. While this changes the cavity length between the waveguide and the pinhole, it also changes the cavity length between the waveguide and the bolometer.

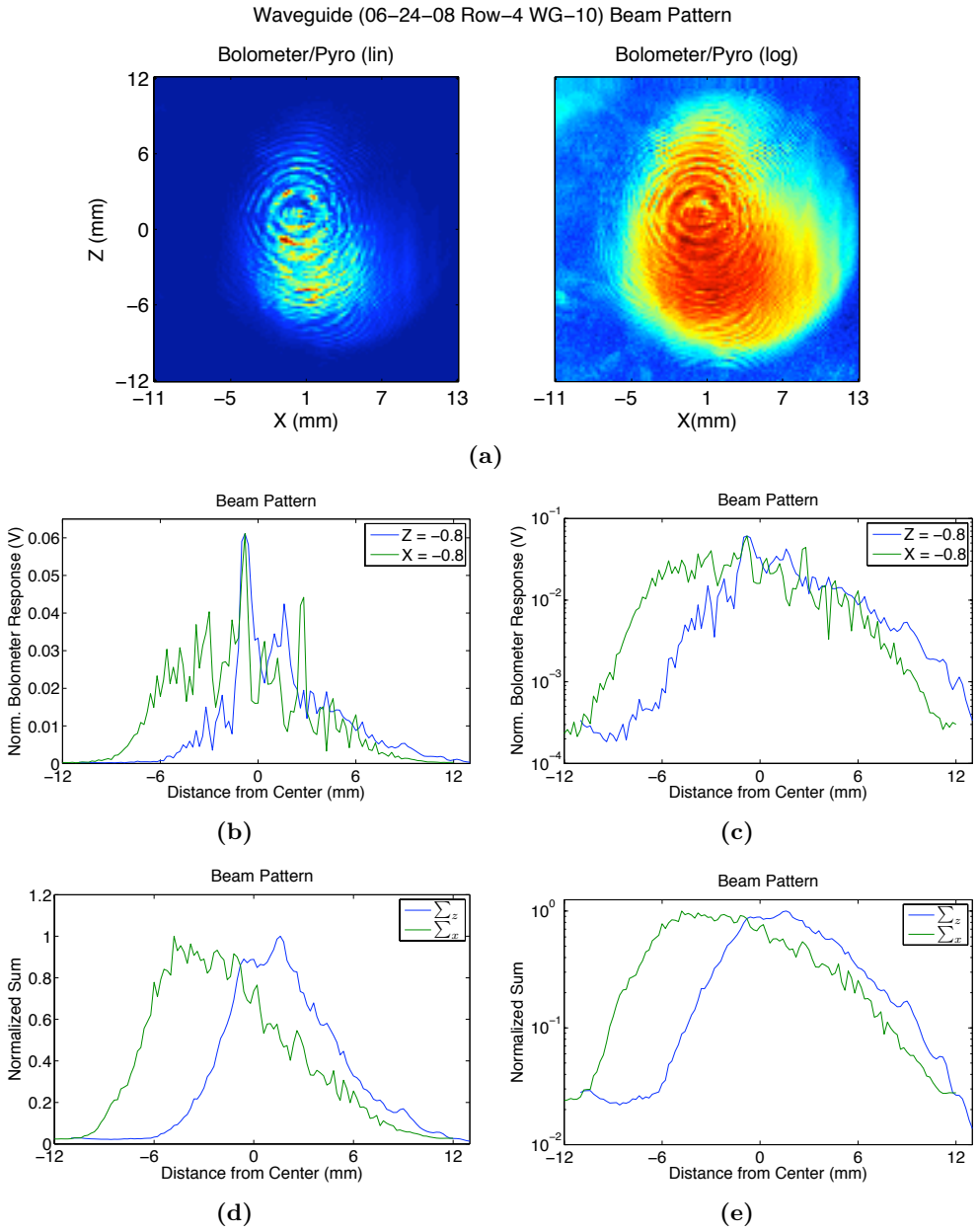

Figure 3.2. (a) Measured beam pattern for waveguide 06-24-08-02-row4-wg10. The image represents transmission through the pinhole scanned over an area of 24 by 24 mm with a step size of 0.2 mm. The outline of a circle in the log scale image shows the effective collecting area of the mirror. The fact that it is not 2 inches in diameter indicates the mirror is not perfectly aligned. (b),(c) show the actual amplitude fluctuations for a single slice through the data in each of the vertical and horizontal directions. (d),(e) shows the result summed over the columns or rows to smooth out the fluctuations and see if the overall divergence is larger in one direction.

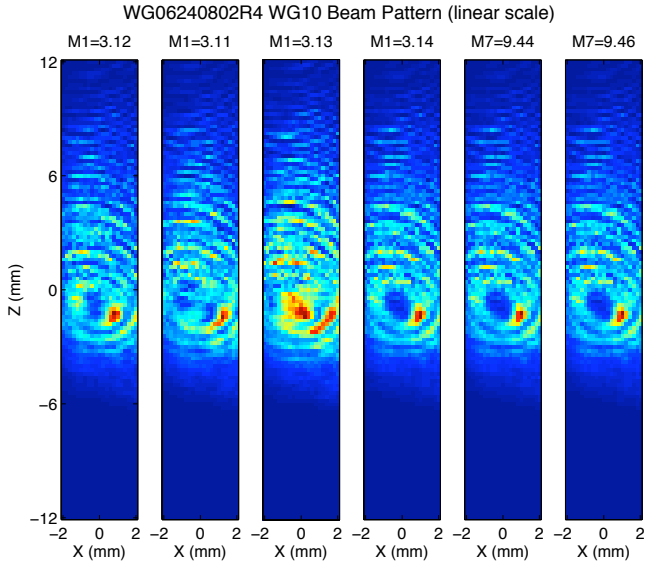

Figure 3.3. Bolometer response to signal transmitting through a pinhole scanning through the emission pattern of rectangular waveguide 10 on sample WG 06-24-08 row 4. Each plot corresponds to movement the waveguide position or the bolometer focussing mirror. (a) original position (M1 = 0.312, M7 = 9.42) (b) M1=0.311, (c) M1=0.313, (d) M1=0.314 (e) M7=9.44, and (f) M7 = 9.46. Note for (e) and (f) M1 was kept at 0.314.

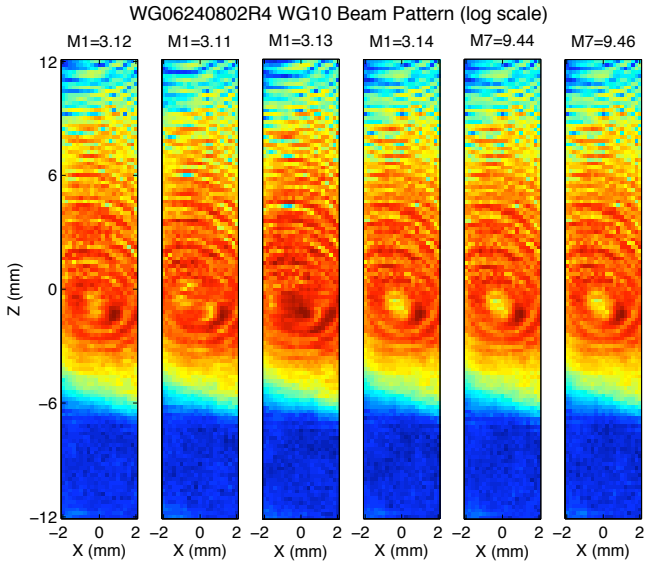

Figure 3.4. Same data as in fig. 3.3 but on a log scale to bring out the low lying signals. The pinhole appears to have been mounted about 6 mm too low as seen by the apparent mirror cutoff at -6 mm.

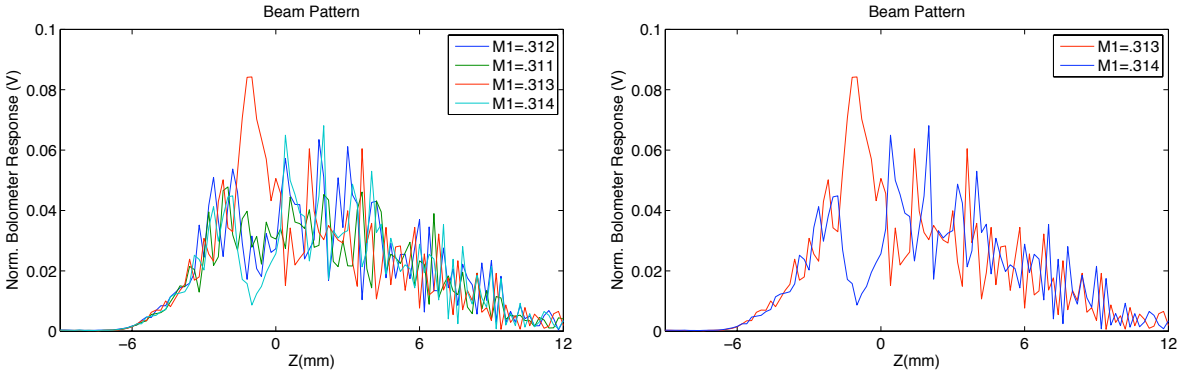

Figure 3.5. (a) Comparison of a vertical slice through the data at $X = 0$ for M1=0.312, 0.311, 0.313 and 0.314 (runs 1-4) (b) M1=0.3

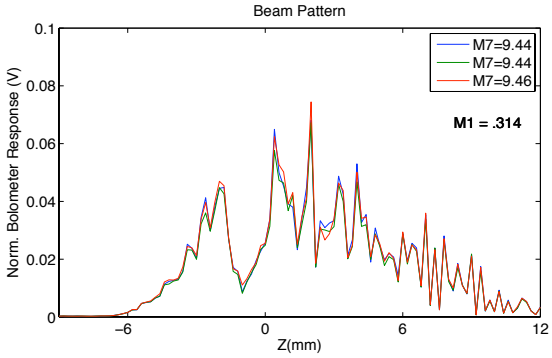

Figure 3.6. Comparison of a vertical slice through the data at $X = 0$ for M7=9.42, 9.44, and 9.46 mm showing that the bolometer distance does not effect the interference fringes.

The 4 leftmost images in Figs. 3.3 and 3.4 show the beampattern for $M1$ = (0.312", 0.311", 0.313" and 0.314") with everything else held constant. Unfortunately, since we reversed direction twice, there is an unknown amount of backlash which prevents comparing the position of the rings, but we can clearly see that the ring patterns are definitely changing phase. Single vertical slices at $X = 0$ are plotted in Fig. 3.5(a). While this looks like random noise, each data set is reproducible so the phase is changing. Fig. 3.10(a) looks at only two slices (M1 = 0.313 and 0.314). The micrometer was moved in the same direction for both of these measurements so backlash should be absent and therefore we can assume the the waveguides moved by roughly 25 microns. For light reflecting off the pinhole mount, back to the waveguide and back through the pinhole, the path length difference compared the light going straight through the pinhole is about 50 microns (ignoring angle effects). This path length difference is nearly $\lambda/2$ so we should expect a phase flip. The data in the plot (within the resolution of the measurement) looks very much like the peaks and troughs have exchanged positions. Thus the waveguide is one of the reflecting surfaces of the cavity creating the interference.

To separate which of the two cavities that involve the waveguide is the one responsible, we also changed the path length of the detection arm without changing the separation between the waveguide and pinhole. The bolometer is not mounted on a translation stage so we could not move it accurately on a 25 micron scale. Therefore we changed the length of the collimated section in the

detection arm by changing focussing mirror distance from the collecting mirror. The micrometer controlling the mirror position along this axis (labelled M7 in the figure) has a resolution of 10 μm per division. The three rightmost images in Fig. 3.3 show the beampatterns for M7 = 9.42, 9.44 and 9.46 mm (at M1 = .314). These images appear to be identical. Fig. 3.6 plots a vertical slice at $X = 0$ from each of the data sets on top of each other to enable more quantitative comparison. There is almost no variation between the scans. This shows that the measurements are quite reproducible, that that oscillations are not due to noise, and that reflections from the bolometer are not significant.

To be thorough we also checked for reflections off the other mirrors. Especially since the first mirror's finite aperture does not collect all the light emitted by the horn, there could also be reflections off of the mirror mounts. However, when we moved each of these mirrors in a similar controlled fashion as above, no change in the fringe patterns was seen. Therefore we attribute the fringe pattern solely to the pinhole position. A cartoon providing a visual image of what we believe is happening is shown in Fig. 3.7. It may be possible that this is the same thing that is happening when others measure QCL beampatterns.

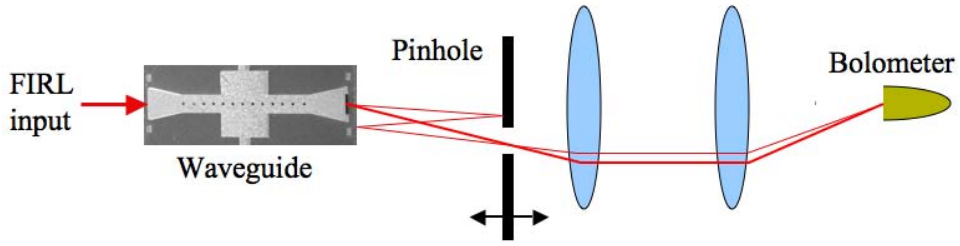

Figure 3.7. Cartoon depicting the interference caused by reflections between the waveguide and the pinhole.

To explore the phase shift in more detail, we measured the beam patterns again as a function of the position of M1 in more detail. To make sure there was no backlash we started by dialing M1 to 0.29" and then back to 0.311" for the initial measurement. The micrometer was increased carefully (so that we did not turn the dial back at any time) for the subsequent measurements. The change in the cavity length and the resulting path length difference for a round-trip of the cavity defined by the pinhole and the waveguide expressed in distance as well as phase are shown in the following table. The positions measured are shown in boldface. For differences in M1 = 0.007" the phase almost returns to itself. Therefore we collected data for two sets of points with that M1 difference. For the last measurement we rotated the bolometer by around 15° instead of moving M1 to confirm that interference pattern was not due to feedback from the bolometer (M1 stayed at 0.319).

2D scans were taken at:

M1 (in.)	**0.311**	**0.312**	0.313	**0.314**	0.315	**0.316**	0.317	**0.318**	**0.319**
ΔM1 (μm)	0	25.4	50.8	76.2	101.6	127	152.4	177.8	203.2
ΔL_{cav}	0	50.8	101.6	152.4	203.2	254.0	304.8	355.6	406.4
L / λ	0	0.434	0.868	1.302	1.735	2.169	2.603	3.037	3.471
Phase (°)	0	156	312	469	625	781	937	1093	1249
Phase (°)	**0**	**156**	312	**109**	265	**60.9**	217	**13.2**	**169**

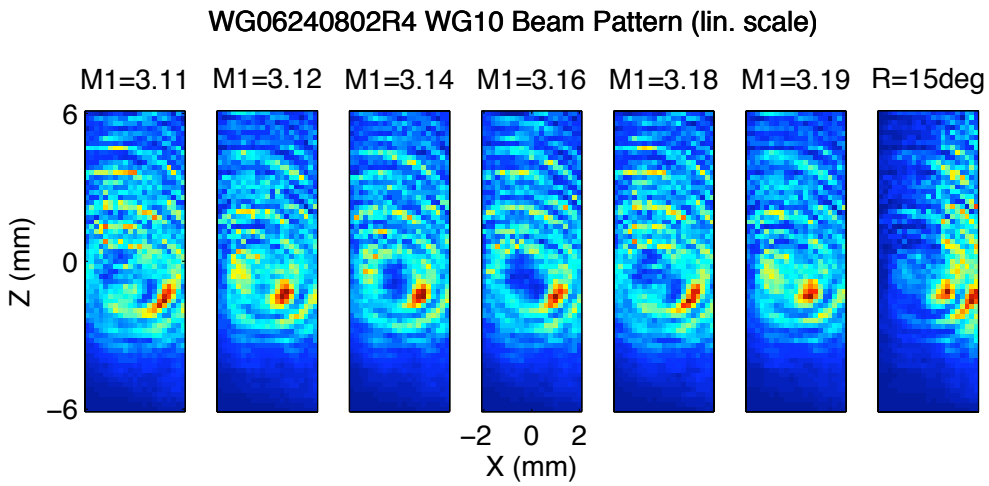

Figure 3.8. Bolometer response to signal transmitting through a pinhole scanning through the emission pattern of rectangular waveguide 10 on sample WG 06-24-08 row 4. The first 6 plots were taken with M1= (0.311, 0.312, 0.314, 0.316, 0.318, 0.319). For the last scan, the bolometer was rotated ∼15 degrees (M1 = 0.319).

Figure 3.8 shows the 2D images for all of the scans. The phase clearly changes throughout the set, and we can see that the images for each pair of points with ΔM1 = 0.007 (3.11, 3.18) and (3.12, 3.19) are nearly identical as expected.

The following figures provide a more quantitative look at the data. Fig. 3.9(a) plots a vertical slice from each of the scans for $X = 0$. We can see that the signal drops a lot when the bolometer is rotated. The rest show similar patterns as above.

Fig. 3.10(b) highlights four of the slices corresponding to different M1 positions. As shown in the table the phase difference between scans (0.311, 0.318) or (0.312 and 0.319) is only 13° and the curves should be similar (which is indeed seen). Also the phase difference between (.311, .312) or (0.318, .319) is 156°. While not perfectly 180° out of phase, 156° is relative close, and we can see that the peak and troughs are roughly inverted again agreeing with expectations.

Fig. 3.9(c) compares the two scans with different bolometer rotations. We can see that at $X = 0$, the signal dropped by a factor of 8, but the interfrence pattern stayed essentially identical. Thus the bolometer orientation is not important in terms of interference. On the other hand, the intensity distribution clearly changed, so the bolometer orientation does effect the envelope of the intensity distribution. This could be a result of blocking some of the beam geometrically by the bolometer apertures, or rejection of part of the radiation because of the finite acceptance angle of the winston cone, or it may just have to do with the reflection coefficient versus angle of incidence on the window. If we continued with this type of measurement we would have had to correct for this effect.

A possible way to remove the interference rings is to sum scans taken 180° out of phase, or to sum a collection of images made up of pairs of scans, each 180° out of phase with each other, but with the pairs corresponding to various angles. The micrometer does not have the accuracy to do

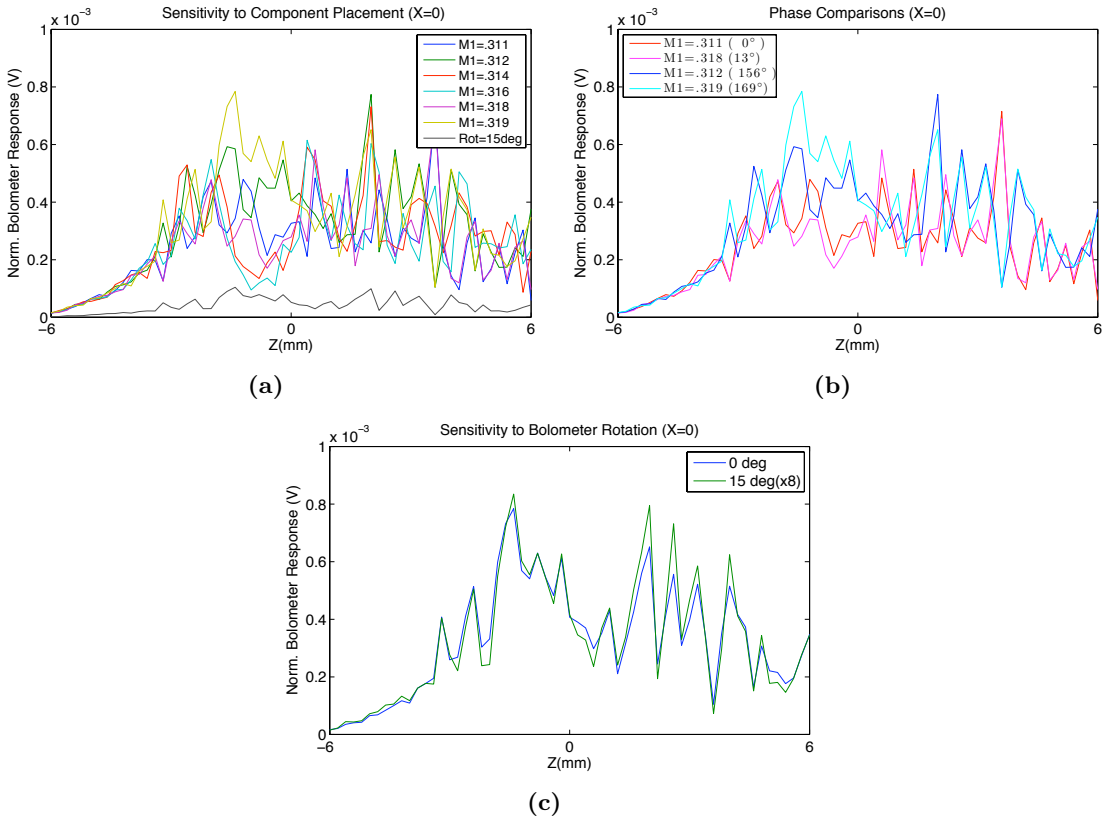

Figure 3.9. Comparison of a vertical slice through the data at $X = 0$ for (a) all runs (b) M1=0.311, .318, .312 and 0.319 only, and (c) the bolometer at 0° and 15°for M1 = 0.319

this precisely, but summing the data over 4 of the runs that are not quite 180° still reduces the oscillation amplitude seen in each individual curve (see fig. 3.10(b)).

Correcting for Phase: Possibly a better way to account for the phase variation is to take multiple scans, but instead of trying to insure the scans are averaged at 180° out of phase with each other, we can fit the acquired data to a sine function of the form $(A + B\sin(M1 + C))$. The offset, A, should correspond to the actual value without interference. This requires taking a number of long scans to get the actual beam pattern, but it should actually work if neccessary. Again putting the detector on an appropriate mount and removing all objects between the waveguide and detector would be better, but even then there might be some feedback from the detector surfaces and this technique would be helpful in this case as well. Note that with the current micrometer, the position of M1 is probably only accurate to within ± 3 μm. For accurate fitting, a better micrometer would be important. It would also be better to take all the data points within one wavelength instead of over 4 periods. However, we decided instead to look for a different method to measure the beampattern.

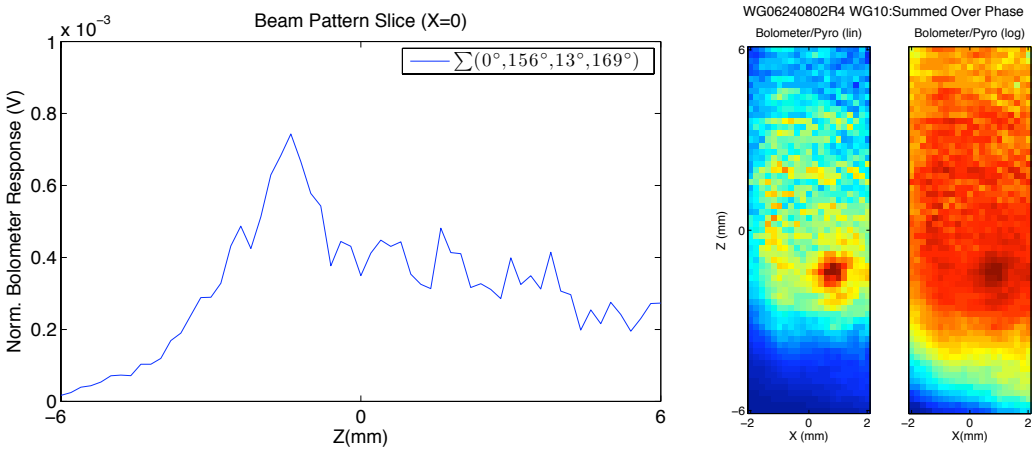

Figure 3.10. (a) Vertical slice through the data at $X = 0$ summed over four runs (M1=0.311, 0.312, 0.318 and 0.319) (b) 2D image of the same sum.

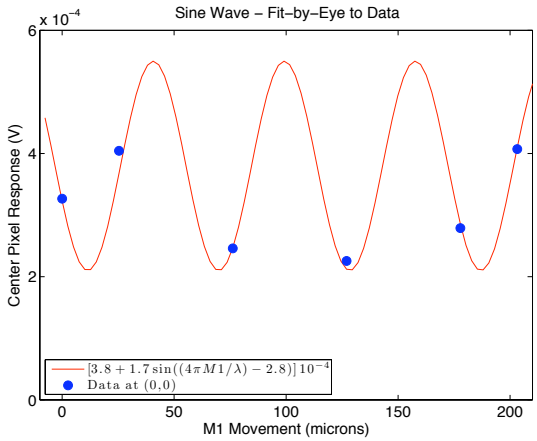

Figure 3.11. Example of a sine wave fit (by eye only) to the data at (0,0) as a function of M1, suggesting that the actual value for the signal at a specific angle can be extracted from images taken at various M1 positions.

3.2 Ideal Beampattern Measurement

Ideally we would move a detector over a half sphere on the output side of the waveguide horn keeping the horn-to-detector distance constant and as well as the angle the detector element makes with respect to the ray connecting it to the horn. Keeping the distance constant eliminates issues of trying to correct for the intensity drop as the beam diverges, while keeping the angle constant ensures that the effective solid angle seen by the detector remains constant and also makes sure that any coupling losses (e.g. due to Fresnel reflections off windows as seen above) will remain constant.

The bolometer has an aperture size of 15 mm. If we just used this as the "pinhole" the bolometer aperture would have to be 860 mm away (nearly 3 feet) to subtend a 1° angle. This is a big arc. A smaller arc is desired. To minimize interference with other optics, it is probably best to design the arc so that the bolometer is always on the output side of the waveguide (see Fig. 3.12(a)). Since the bolometer is almost 9 inches in diameter, the center of it should never be closer than 4.5 inches to the dotted line in Fig. 3.12(a). In this case, the maximum angle that can be measured versus the distance from the waveguide to the bolometer window is

$$\Theta = \sin^{-1}\left(\frac{4.5}{x+4.5}\right), \tag{3.1}$$

where x is the distance between the waveguide and the bolometer window. The maximum angle and the pinhole size corresponding to a 1° capture angle (assuming it is at the same distance as the bolometer window) is plotted in Fig. 3.12(b) . For the distances plotted, the pinhole is significantly larger than a wavelength so that diffraction effects should be minimal.

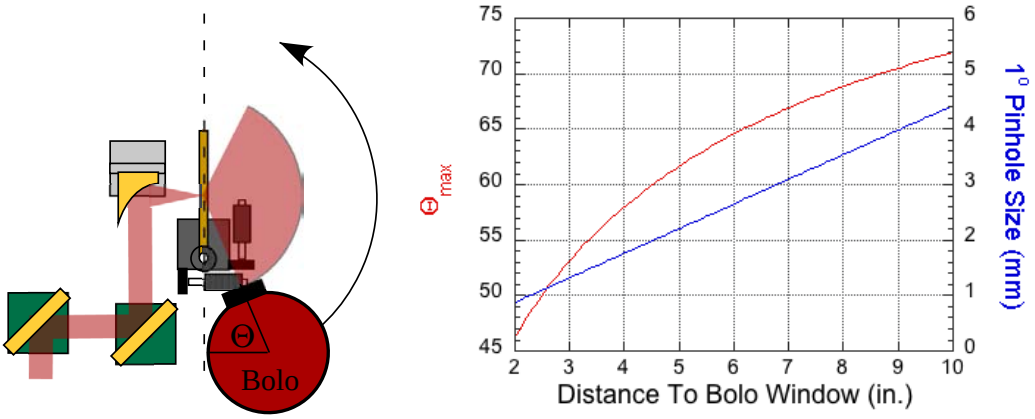

Figure 3.12. (left) Geometry of optics. (right) Maximum captured angle and required pinhole size as a function of distance between bolometer window and waveguide.

Unfortunately, it is not really practical to move a bolometer around accurately over a half-sphere. The bolometer is extremely heavy and bulky and it would be difficult to move it along even a simple horizontal arc. In addition, tipping the bolometer could lead to cryogen spilling. Thus moving the bolometer up and down is not really practical (especially over many degrees of arc). Assuming we could only move the bolometer along an arc in a horizontal plane as shown in Fig.

3.12, we could still measure the full beampattern by rotating the sample so that the horizontal arc is measuring arcs through the center of the beampattern along different angles. (See Fig. 3.13). In this case, the center will have a lot of duplicate data since the finite aperture of the pinhole will overlap between scans. For this to work the waveguide must be rotated about its center to keep the aperture in the same place. In addition, since the waveguide is polarization dependent, we would need to rotate the input laser polarization as well to prevent the signal from decreasing as the cosine of the angle.

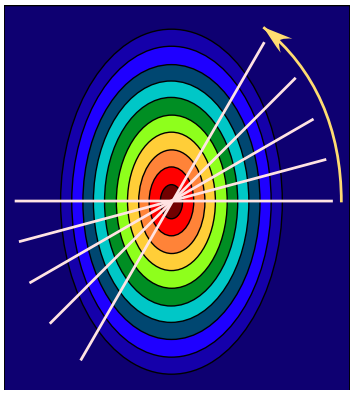

Figure 3.13. Rotating the sample allows measurement of the beampattern while only moving the detector along a single path. However, the measurement density will vary with distance from the center.

Given the time and resources available, we did not deem this to be a realizable approach. No commercially available rotation stages exist that can move a 60 pound bolometer, let alone with 1° accurately and reproducibly. In addition, THz polarization rotation optics are also not commercially available so it would be hard to maintain input coupling to the waveguides. Lastly, because the waveguides do not terminate at the end of the substrate holding them, they do not radiate directly forward so the beampattern would not be centered where all the scans intersect as depicted in Fig. 3.13. Besides not providing the best data near the center of the beampattern, it would be much harder to normalize the curves if the interection between curves were not all at the peak of the beampattern.

3.3 Indirect Beampattern Measurement

An alternative method to measure the beampattern is to build a half-paraboloid to capture and collimate almost all the angles emitted by the waveguide. Then scanning a detector over a 2D plane perpendicular to the beam propagation in the collimated section of the beam (as depicted in Fig. 3.14) will provide an image related to the actual beam pattern. Moving a detector over a 2D plane is much easier to achieve than scanning over an arc. To measure the beam pattern over all angles requires a half-paraboloid since standard off-axis paraboloids only capture a fraction of the total 2π steradians - e.g. even when using a 'F/1' optic the total collection angle in one plane is only 59° and 74° in the other (see Fig. 3.15). With a hemi-paraboloid, we capture nearly all 180° in one direction and more than 90° in the other (depending on how wide the mirror is)(see Fig.

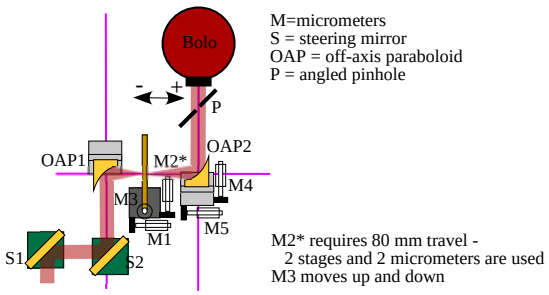

Figure 3.14. Optical set-up for beam-pattern measurements.

3.16). Technically the mirror does not need to be any wider than the effective focal length (EFL), since we can measure one half of the beam pattern, rotate the sample 180 ° and measure the other half of the beam pattern. However, a little mirror extension would help in the data combining, and if the beam divergence is not that large it could be measured all at once without rotating the sample.

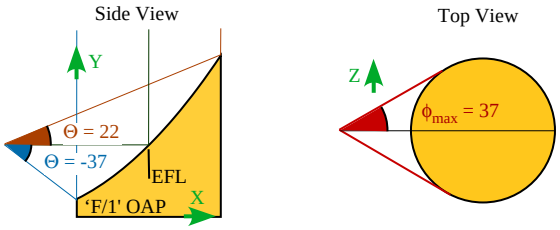

Figure 3.15. Angles collected by a standard 'F/1' off-axis paraboloid.

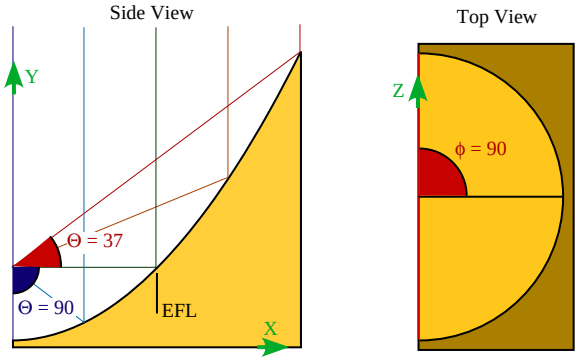

Figure 3.16. Angles collected by a hemi-paraboloid that is twice as wide as the effective focal length (EFL).

There are a few issues with this method.

- The scan does not directly measure the beam pattern. The measured 2D pattern has a 1-1 correspondance with the beam pattern, but requires a mathematical transform to extract the true pattern.
- The mathematical transform is accurate only if (i) the waveguide horn lies at the focal point of the mirror, and (ii) we ignore divergence. The first requires precise alignment, while the second requires measurement in the collimated beam after a very short propagation length.

- There is always some part of the beam at large positive angle striking the pinhole directly, and this could interfere with the light bouncing off the mirror unless a baffled pinhole, or an angled pinhole plate is used to prevent this non-collimated ray from hitting the detector.
- Since the beam is not continually expanding, we will again need a small pinhole to achieve 1° accuracy, unless the mirror is large.
- The effective angular area captured by the pinhole depends strongly on position of the pinhole.

To get an estimate of the pinhole size required versus mirror size, we can look at a couple examples. For $\phi = 0$,

$$\tan\Theta = \frac{\Delta y}{\Delta x} \tag{3.2}$$

$$= \frac{y(x) - y(f.p.)}{x} \tag{3.3}$$

$$= \frac{\frac{1}{2EFL}x^2 - \frac{EFL}{2}}{x} \tag{3.4}$$

$$\tan\Theta = \frac{1}{2}\left(\frac{x}{EFL} - \frac{EFL}{x}\right). \tag{3.5}$$

$$\tag{3.6}$$

Where EFL is the effective focal length and $y(f.p.)$ is the height of the focal point which is $1/EFL$. Figure 3.17(a) plots x versus Θ. The flattest slope, near $-90°$, gives a change of $(0.009\,EFL)$ per

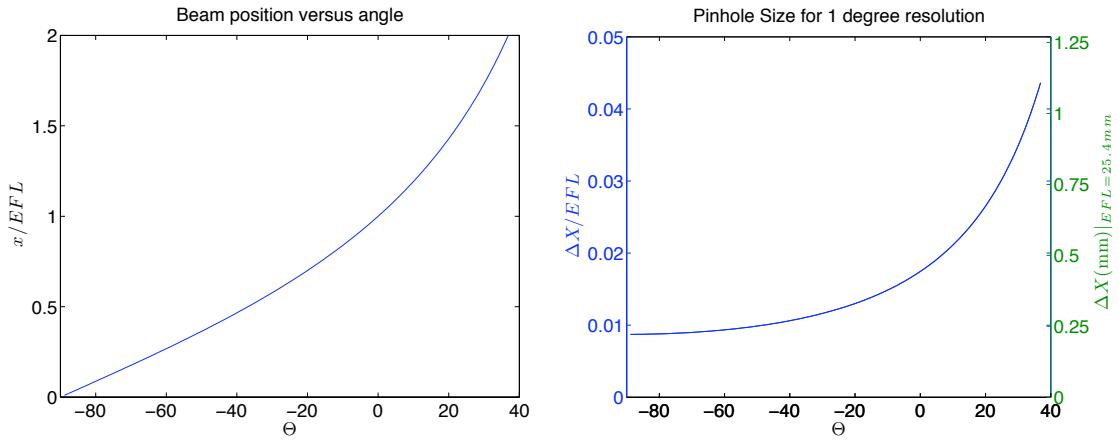

Figure 3.17. (left) Final X-position of rays depending on Θ. (right) The change in the x-position for a 1° change in Θ as a function of Θ.

degree. The instantaneous slope for the whole curve is found by differentiating the above to yield:

$$\sec^2\Theta d\Theta = \frac{1}{2}\left(\frac{1}{EFL} + \frac{EFL}{x^2}\right)dx. \tag{3.7}$$

Thus for $\Delta\Theta = 1°$:

$$\Delta x = 2\sec^2\Theta\left(\frac{1}{EFL} + \frac{EFL}{x^2}\right)^{-1}. \tag{3.8}$$

Figure 3.17(b) plots $\Delta x|_{\Delta\Theta=1}$ as a function of Θ. This confirms that the most negative angles will define the maximum pinhole size. For a 1 inch effective focal length a pinhole smaller than 225 μm is needed to maintain 1° accuracy. This is less than 2λ, so throughput would be low and diffraction effects may make it impossible to separate the reflected and direct incidence beams with baffles. Therefore a larger mirror is desirable.

3.3.1 Pinhole Size Effects

One thing that has been neglected so far is the diffraction pattern (Airy pattern) of the pinhole. For measurements involving use of parabolic reflector, light may enter the pinhole via two routes. (see Fig. 3.18). The first is the desired path reflected by the mirror. The second is direct incidence on the pinhole from the waveguide horn. Light going through the pinhole will be diffracted and emit into a cone of light on the backside of the pinhole. If the detector is positioned so that we collect all the desired light, then to prevent interference the undesired cone cannot overlap the desired cone at all. This means that the angle ϕ of the direct ray, must be greater than twice the angular width of the diffraction (θ) as depicted in the figure.

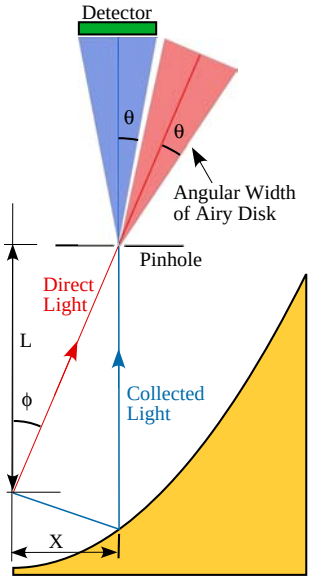

Figure 3.18. Cartoon of potentially interfering beam paths incident on a pinhole after light from a emitting source is collected by a reflective parabaloid. The colored triangles represent the width of the Airy disk after diffraction by the pinhole..

For a circular hole the diffraction pattern is given by

$$\frac{I}{I(0)} = \left[\frac{2J_1(ka\sin\theta)}{ka\sin\theta}\right]^2 \tag{3.9}$$

where, $k = 2\pi/\lambda$, a is the radius of the hole, and I is the intensity. This function is plotted as a function of $ka\sin\theta$ in fig. 3.19(a). This pattern extends to infinity, but most of the light resides in the central peak. Therefore we have to decide at what point the intensity of the unwanted beam is

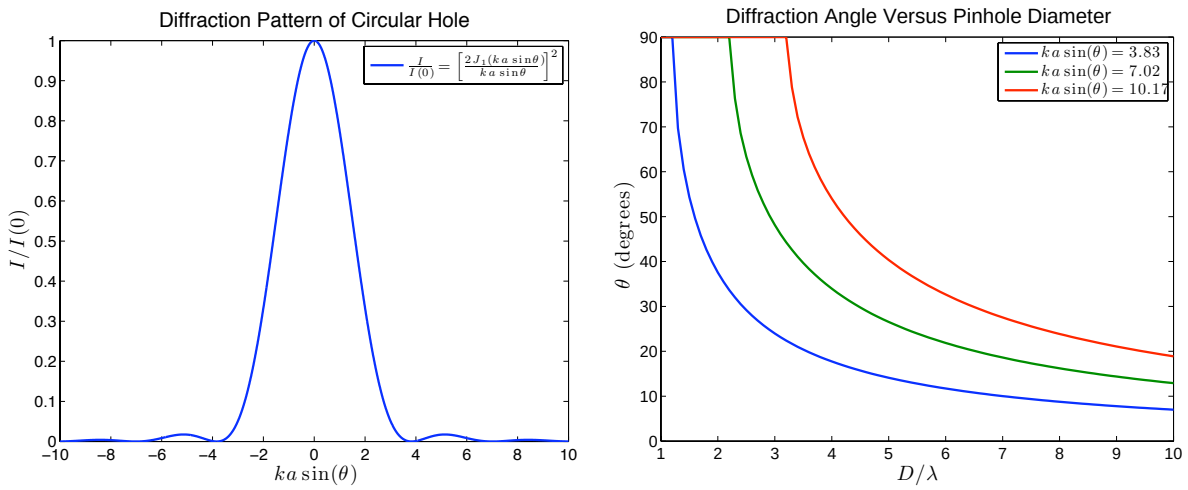

Figure 3.19. (a) Radial dependence of diffraction (Airy) pattern caused by the pinhole. (b) Angular width of the diffraction pattern from the center to the 1st, 2nd and 3rd zero of the Airy pattern.

small enough that we do not care about it anymore and define this angle as the cone width. The peak intensity of first side lobe is only 2% of the central lobe which is fairly negligable. Therefore, for the argument below we chose theta to be the angle that corresponds to the first 'zero' of the Bessel function in Fig. 3.19(a), i.e. when $ka\sin\theta < 3.83$. Rewritting to give θ in terms of D/λ, we get

$$\theta = \sin^{-1}\left[\frac{3.83}{\pi}\frac{\lambda}{D}\right]. \tag{3.10}$$

This expression for θ corresponds to the lowest curve in Fig. 3.19(b). The other two curves show the cut-off angle for the second and third zero of the Bessel function respectively.

As mentioned above, to achieve 1° accuracy, with a 1 inch EFL, the pinhole would need to be on the order of 250 μm ($\sim 2\lambda$). Looking at Fig. 3.19(b), we can see that in this case the Airy disk has an angular width of nearly 35°, which requires that $\phi > 70°$. Essentially this means that every ray incident directly on the pinhole will be seen by the detector. Figure 3.20 plots ϕ assuming $L = 2 \times EFL$, which puts the pinhole just a little bit outside the mirror.

For larger L, ϕ decreases which means that more of the light incident on the pinhole directly will hit the detector element. This would be bad if the radiation source was isotropic. However, the radiation pattern from the horn is not isotropic, so the fractional intensity emitted into small ϕ may be quite small to begin with. In this case, interference of the direct rays with the relfected rays should be negligable. This will depend on the orientation of the horn, but from the models, the H-plane cut should have a beam width less than 30 degrees, so that most of the intensity will hit the mirror and little will hit the pinhole directly, especially as the pinhole is moved further from the mirror. Moving the pinhole away will also minimize the impact of the direct ray due to the fact that the direct beam intensity will drop as $1/R^2$, while the collimated beam will have significantly lower loss.

Given the cost and difficulty of obtaining a large half paraboloid we started out just using a

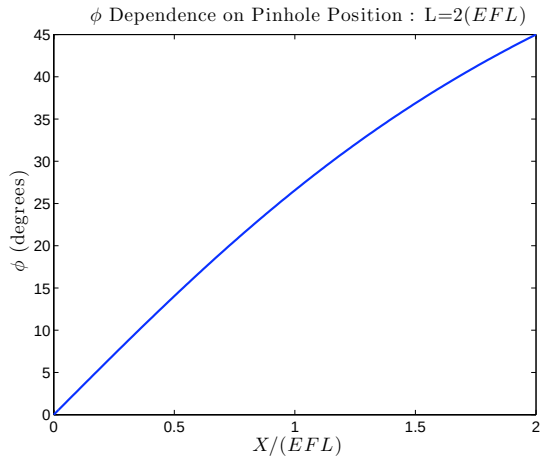

Figure 3.20. The dependence of ϕ on the x-position of the pinhole, for a paraboloid given by the expression $y = \frac{1}{2(EFL)}x^2$

standard off-axis mirror. This will limit the collection angles as we did with the prior measurements discussed above. The two big advantages of this measurement technique over the previous one is that the pinhole can now be tilted enough so that the reflected beam is dumped (and therefore cannot interfere) and that the ray hitting the detector always hits the detector at the same angle and position on the window. A cartoon showing this arrangement is shown in Fig. 3.21 (although in reality a OAP is used instead of a refractive lens). In principle a refractive lens as shown in the cartoon could also be used and would eliminate the problem of having two paths to the detector. However, in this case the captured angle would very be limited, and the lens would have to have a really good anti-reflection coating to prevent interference fringes again. All the following data have been taken with this arrangement.

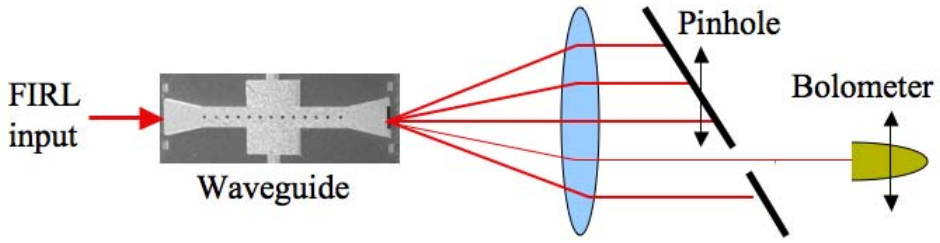

Figure 3.21. Cartoon depicting the essential elements for measuring the beam pattern without interference effects due to back-reflections from the pinhole. The pinhole and bolometer move together.

3.3.2 Expected 2D patterns

As mentioned above, the OAP will map the beampattern into a pattern that is not intuitive. Therefore it is instructive to first show what the beam patterns should look like. From HFSS modeling, the far-field pattern from the waveguide should be fairly narrow in the horizontal direction and fairly wide in the vertical direction. Thus if the beam was incident directly onto a wall we would expect to see a roughly vertically oriented ellipse.

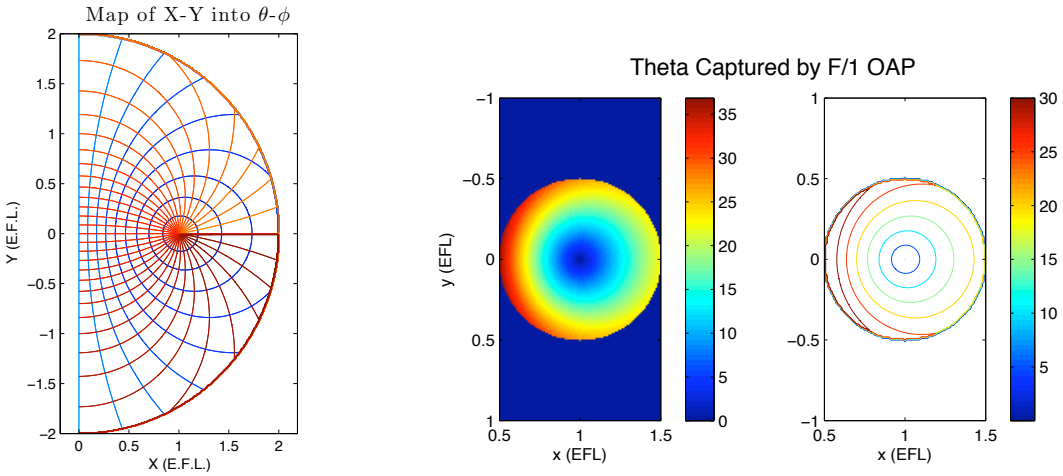

Figure 3.22. (a) The mapping of rings of contstant θ (10° intervals in blue hues) and curves of constant ϕ (10° intervals in red hues) onto a 2D planar surface after reflection by a hemi-paraboloid. (b) The angular width of a standard "F/1" off-axis paraboloid.

Figure 3.22(a) shows what happens to the curves of constant θ and constant ϕ once they reflect off of an hemi-paraboloidal mirror with an overall radius that is twice the effective focal length. Before reflection, curves of constant θ are circular and concentric while lines of constant ϕ radiate linear out from the center. After the mirror however, we can see that curves of constant θ are circular but not concentric, while the "lines" of constant ϕ are no longer straight. Fig. 3.22(b) shows the angles we can capture using a conventionally available off-axis paraboloid that has a diameter equal to its focal length (psuedo-F/1 mirror). This mirror corresponds to the one used in the measurements with the effective focal length equal to 2 inches. Clearly, using a standard mirror significantly reduces the amount of the beampattern that can be measured.

The previous figures only show the mapping of the angular emission onto a 2D planar surface. However, they do not show what an actual beam will look like. To get an better idea it is instructive to go through a progression of potential input beams. As an ideal case, Fig. 3.23(a) shows what an ideal circularly symmetric Gaussian beam would transform into at the planar surface. Because the 37 x 400 μm aperture is sub-wavelength in one dimension and multiple wavelengths in the other, the beam is better approximated by an elliptical Gaussian. The mapping of an elliptical Gaussian is shown in Fig. 3.23(b). The image does not appear elliptical anymore but looks more kidney shaped. We also know that the elliptical pattern will not be centered with respect to the boresight

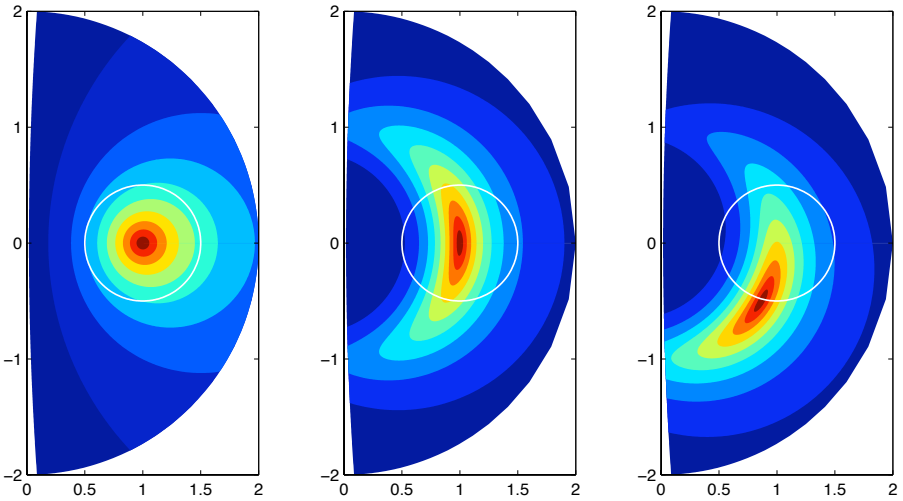

Figure 3.23. Beamshape appearance on a 2D plane after reflection off of a parabolic reflector assuming an input beam that is (a) Gaussian, (b) elliptical Gaussian, and (c) elliptical Gaussian directed downward at 30 degrees. The white circles correspond to the portion of the beam pattern that would be captured by an F/1 OAP.

of the waveguides because of the finite substrate lip in front of the apertures. Assuming a 30° tilt, the peak intensity of the image shown in Fig. 3.23(c) nearly moves off the edge of a standard OAP (represented by the white circle).

Assuming that everything is aligned properly in the measurements we should expect something similar to this last image. Unfortunately, especially since one cannot see the beam, perfect alignment is not guaranteed. Therefore in Fig. 3.25 we show the consequences of slight misalignments. There are 6 images, each one represents a translation of the waveguide aperture by 1 mm from the true focal point of the mirror. The axes for these movements is depicted in figure 3.24.

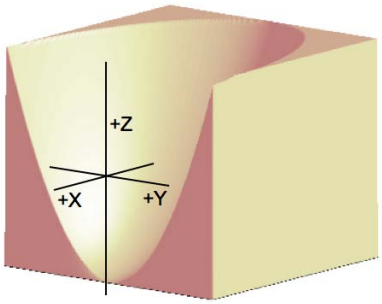

Figure 3.24. Cartoon Image of paraboloidal mirror with direction axes defined. θ is the angle between the $-x$ axis and the ray emitted from the origin. ϕ is the angle the a projection of the emitted ray makes with respect to the $+z$ axis.

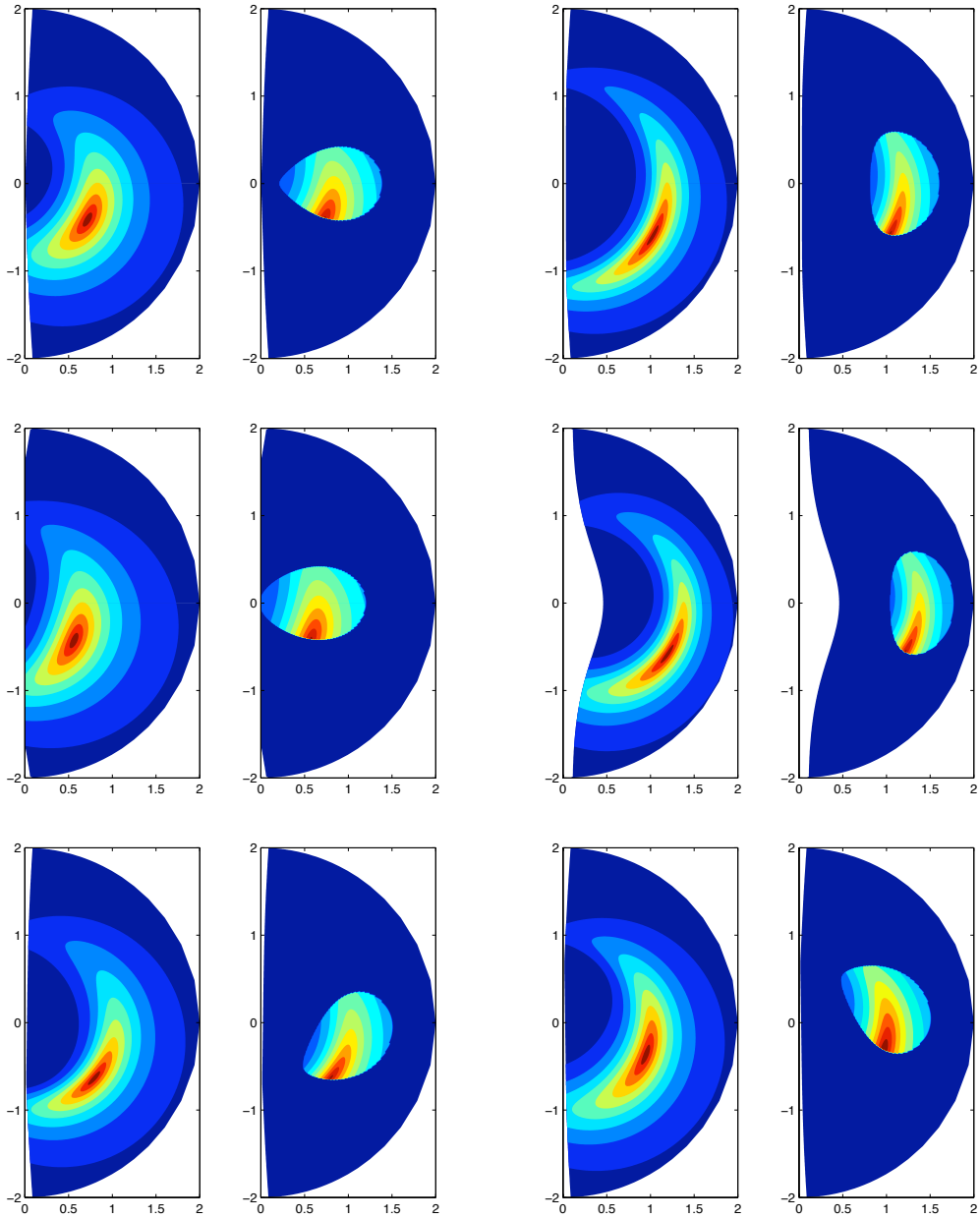

Figure 3.25. The beam distortion if the waveguide moves plus (left) or minus (right) 1 mm in the Z direction - (top row) , X direction (middle row) or Y direction (bottom row). The right hand image of each pair shades everything that does not hit an F/1 OAP.

3.3.3 Measured Beampatterns

Unfortunately, we were unable to finish working all the kinks out of this measurement and did not obtain beampatterns that we trust at this point. The following images provide some representative images. The beam distortions shown in fig. 3.25 can be seen in some of the actual measurements. However, even when the outline of the mirror appears circular the shape does not look like what we expect. Sometimes there we're strong oscillations in these images as well. Suggesting that there is still some feedback present.

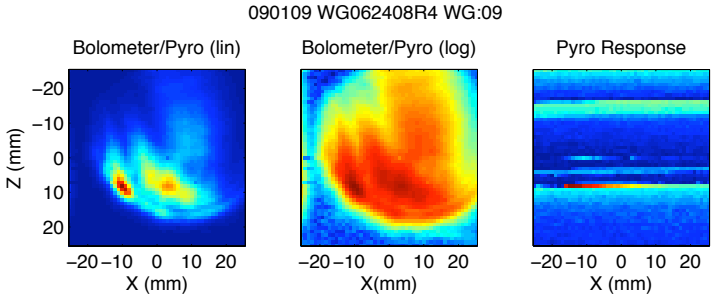

Figure 3.26. Measured beampattern of waveguide with standard horn shape at 2.56THz.

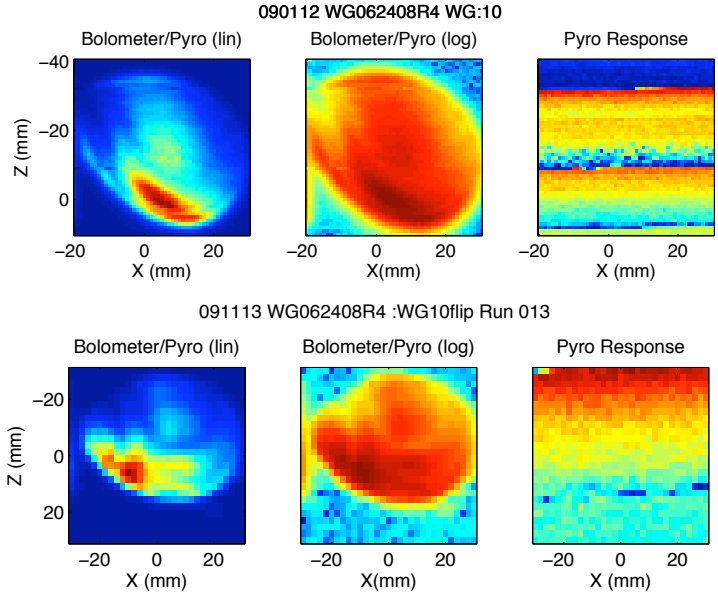

Figure 3.27. Beampattern of similar waveguide. In the top image the collection mirror had been moved along the Y axis between acquisition of this image and the last. In the bottom image the collection mirror was moved back to its original Y position but the X position of the waveguide was moved. The beam distortion is clearly seen ouline of the mirror is clearly seen.

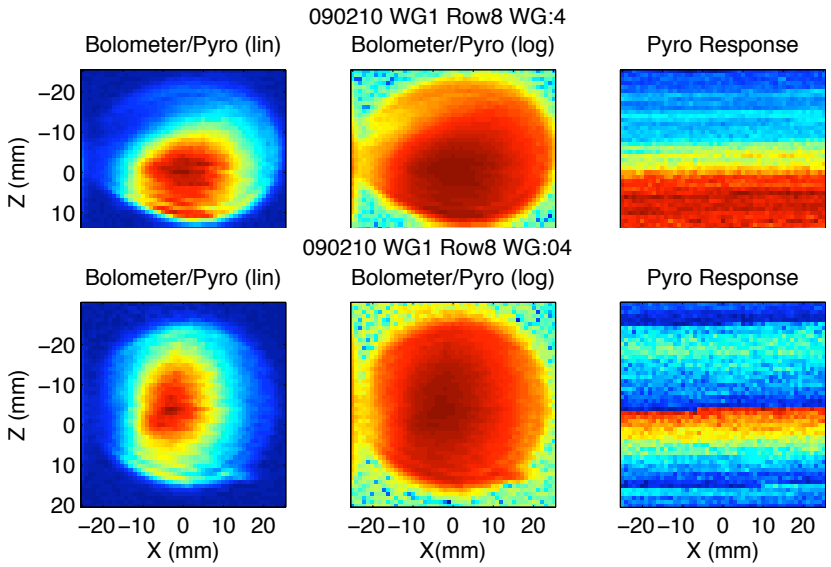

Figure 3.28. Image of a WG from a completely different chip. The beam appears to be much more centered - it is possible this is due to a smaller substrate lip in front of the horn aperture. The distance to the collection mirror was adjusted between the scans so the mirror image in the log plot appears more circular.

Chapter 4

Integrated Lasers with Rectangular Waveguides

4.1 Thermal expansion mismatch induced failure mitigation

One of the first steps in this project was to reduce the stress induced failures caused by differential thermal expansion of the horns and the carrier substrate. These failures were due to the relatively large thermal mismatch between the GaAs substrates required for the lasers and the gold rectangular waveguides (5.8 vs 14 [10^{-6}/K @ 20 K] respectively). In previous work on laser-waveguide integration, the the first generation lasers were embedded in a thick layer of plated gold. When cooled to cryogenic temperatures, the GaAs surrounding the laser cracked. Sometimes the laser would still be weakly attached but the poor thermal conduction prevented them from working anymore, but more often they just flaked off, leaving a crater in the carrier substrate below the original laser position. Cracking around the waveguides in this first generation was not observed.

The second generation of integrated designs, completed at the very end of the previous project, removed the thick metal layer above the lasers, but did not change the waveguides. No cracking was observed around the lasers this time, but unfortunately, significant cracking was observed around the rectangular waveguides. This was a bit of a suprise, since no cracking was observed around the horns on the first generation samples. It is possible that the craters observed around the lasers in the first generation released enough stress to prevent cracking around the horns, or we just were not looking close enough.

The ideal solution to this problem would be to use a metal that has the same thermal coefficient of expansion (TCE) as GaAs, but there are only a few alloys that satisfy this condition (W/Cu, 90/10 is one). Unfortunately, we do not yet have the ability to plate these types of alloys and these materials typically have lower conductivity which would lead to significantly higher waveguides losses. In principle the latter problem could be mitigated by plating the inner layers with a thin layer of gold to provide high conductivity walls and overplate with another material with good structural and TCE properties, but this level of effort was outside the scope of the project.

Therefore, during this project (starting in revision 4 of the integrated waveguide maskset), we decided to try different geometries of the waveguide walls. This revision was intended to address the cracking that seemed to originate at the antenna corners. It replaced the standard 70 μm wide walls of the waveguide and the sharp corners in the antenna design with a design with thinner walls (scalloped on the outside) and rounded corners. The design is intended to reduce stress concentration at sharp corners and reduce the total area of gold in contact with the GaAs substrate. Because time did not allow for thermal stress modeling, this design is a best guess.

For laser integration only a couple square centimeter piece of active material is bonded near the center of a 3 inch carrier substrate. We can do what we want with the rest of the carrier substrate. Therefore, for this mask set, the regions outside of the active device area, previously occupied with H shaped fill structures, (used to balance the plating load), was instead filled with a set of waveguides with different scalloping structures and wall thicknesses to experimentally evaluate the effectiveness of the new antenna designs, as shown in Fig. A.7. On this mask, 24 different waveguides grouped into a 2x12 array (shown in Fig. 4.4) was repeated many times. The array includes structures with and without end caps, with different magnitudes of scalloping, and with different wall thicknesses.

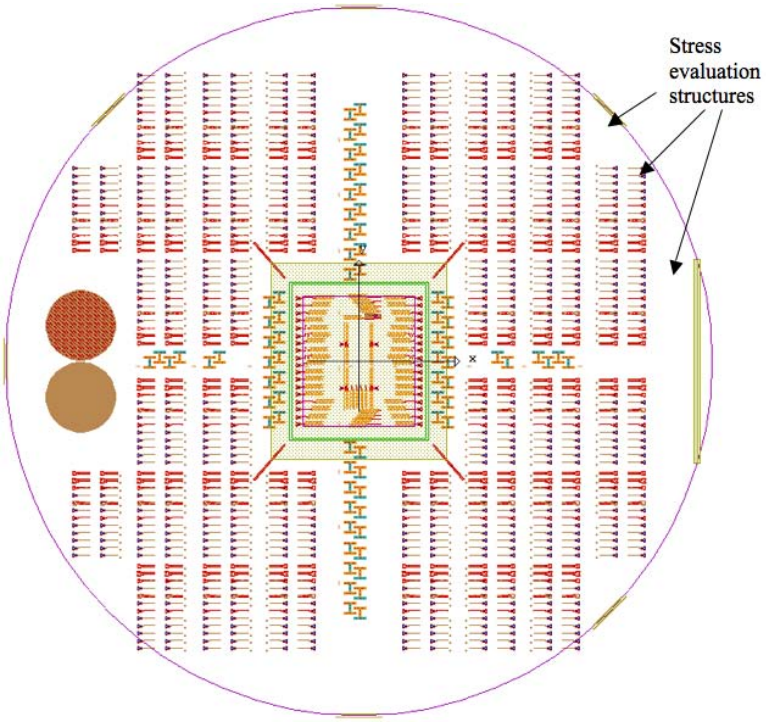

Figure 4.1. Overall mask layout with stress evaluation structures around the active lasers in the center.

To test the arrays of waveguide geometries, we fabricated a full wafer of waveguides on a 3 inch GaAs substrate using the new mask revision. Since we only wanted to test the thermal stress of the carrier substrate, we were able to use a bare GaAs substrate. After fabricating the waveguides, we diced up the wafer into pieces for testing (see Fig. 4.2). We soldered the GaAs chips to copper submounts as we would if we were mounting actual lasers, attached them to the coldfinger in the cryostat, and cooled the coldfinger to 4 K. After warming the samples back to room temperature we examined them for cracking. The diced pieces that we cooled are labelled by a letter in Fig. 4.2. The waveguides that cracked are denoted by an x placed next to the horn.

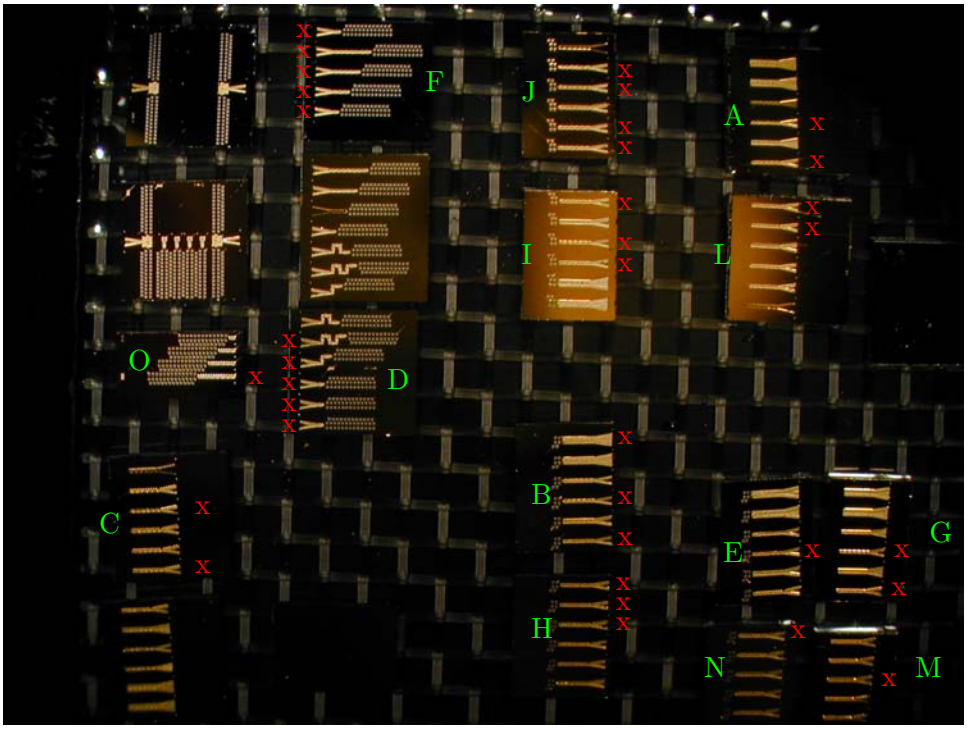

Figure 4.2. Picture of the diced apart waveguides created on a bare GaAs substrate used for testing substrate cracking due to TCE mismatch between the gold waveguides and the GaAs substrate. The green letters denotes pieces that were cooled to 4K and the red x's denote which waveguides cracked due to thermal stress.

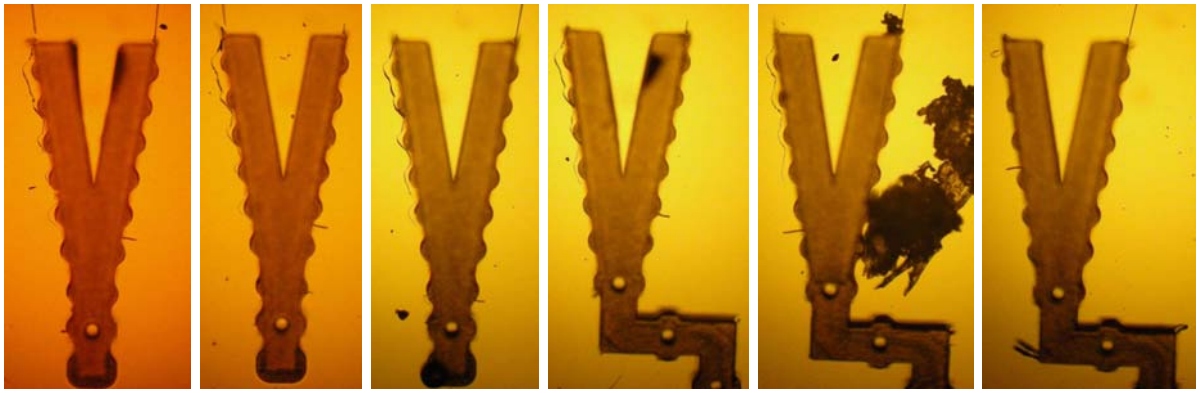

Figure 4.3. Optical microscope pictures of the horns from piece D. A nearly identical crack in the substrate is observed on the left side of 5 of the 6 waveguides. The straight lines above the waveguides are not cracks in the substrate - instead they are the result of a small amount of plating on the substrate where the photoresist cracked.

All but one of the tested horns that were designed to mate with a QCL failed (chips **D** and **F**). Optical microscope images of the horns for chip **D** are shown in Fig. 4.3. The crack on the left side of the waveguide is nearly identical for all of the horns. All of the cracks appear to originate at the upper left corner of the horn (the straight lines that look like cracks actually are not - see Fig. 4.6). While we did thin the width of the metal wall and therefore should have less overall stress, the ends of the waveguides are very narrow and hence even though they are rounded, we created sharp stress concentrators.

The waveguides on chip **O** also mate with QCLs but they were designed for vertical emission and did not terminate into a horn structure. The lack of a horn structure means that the corners were rounded and hence there were no sharp stress concentrators on these waveguides. Only one of these 3 failed (the longest one).

The remaining pieces cover all the different geometry test cases shown in Fig. 4.4. The only difference between the left and right column is a small section of metal connecting the two waveguide sidewalls at the left end of the waveguides (referred to as an endcap). Only 4 waveguides appeared to crack on the left end of the waveguides (2 on piece **J**, 1 on piece **L** and 1 on piece **N**). I have not included these in the following discussion.

Only 1 of the 5 waveguides of the original design failed (70 μm wide walls and square corners). This was unexpected since nearly all of the waveguides of this design integrated with real lasers cracked. The one that failed this time was one of only two waveguides that not only cracked the substrate but completely broke off the wafer suggesting these still have significant amounts of stress. No cracks were seen on the waveguides with the same wall width but rounded ends. Thus just having a lot of metal in contact with the GaAs does not seem to be the main cause for cracking.

Contrary to initial expectations, the thinnest waveguides (or at least the waveguides with the thinnest tips) failed the most. Since these have the least amount of metal contact I thought these would have the least stress. However, the tips are very sharp which must result in a large stress concentration. The straight-walled waveguides with 10 micron tips all failed. The scalloped walls (still 10 μm wide tip at the horn terminus) had a higher survival rate as the magnitude of the scalloping increased from 12.5 μm (1 out of 5) to 20 μm (3 out of 6) to 50 μm (5 out of 6). Therefore it appears the a large scallop will mitigate the stress concentration enough at the tips to prevent the cracks. One set of waveguides had the scalloping out of phase compared to the rest, and for this set only 1 out of 6 survived instead of 3 out of 6 for the other phase waveguide with the same scalloping magnitude, indicating that placement of the scallop also important.

The waveguides with rounded ends and wall widths ≥ 20 μm at the terminus of the horns had the best survival rate. 4 out of 5 of the 70 μm wide walls survived, 11 out of 11 of the 50 μm wide walls at the tips (5 straight, 6 scalloped) survived, 4 out of 5 of the straight 22.5 μm wide walls survived and 5 out of 6 of the 20 μm wide scalloped walls survived. Thus it appears that the best waveguide to use is one with corners with a radius of curvature, $10\mu\text{m} < r < 25\mu\text{m}$. The upper bound is not because of failure at larger radius but just because there will always be more accumulated stress with more metal and it appear that this radius is already large enough.

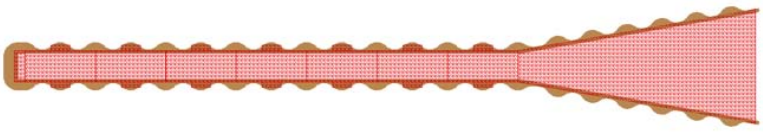

(a)

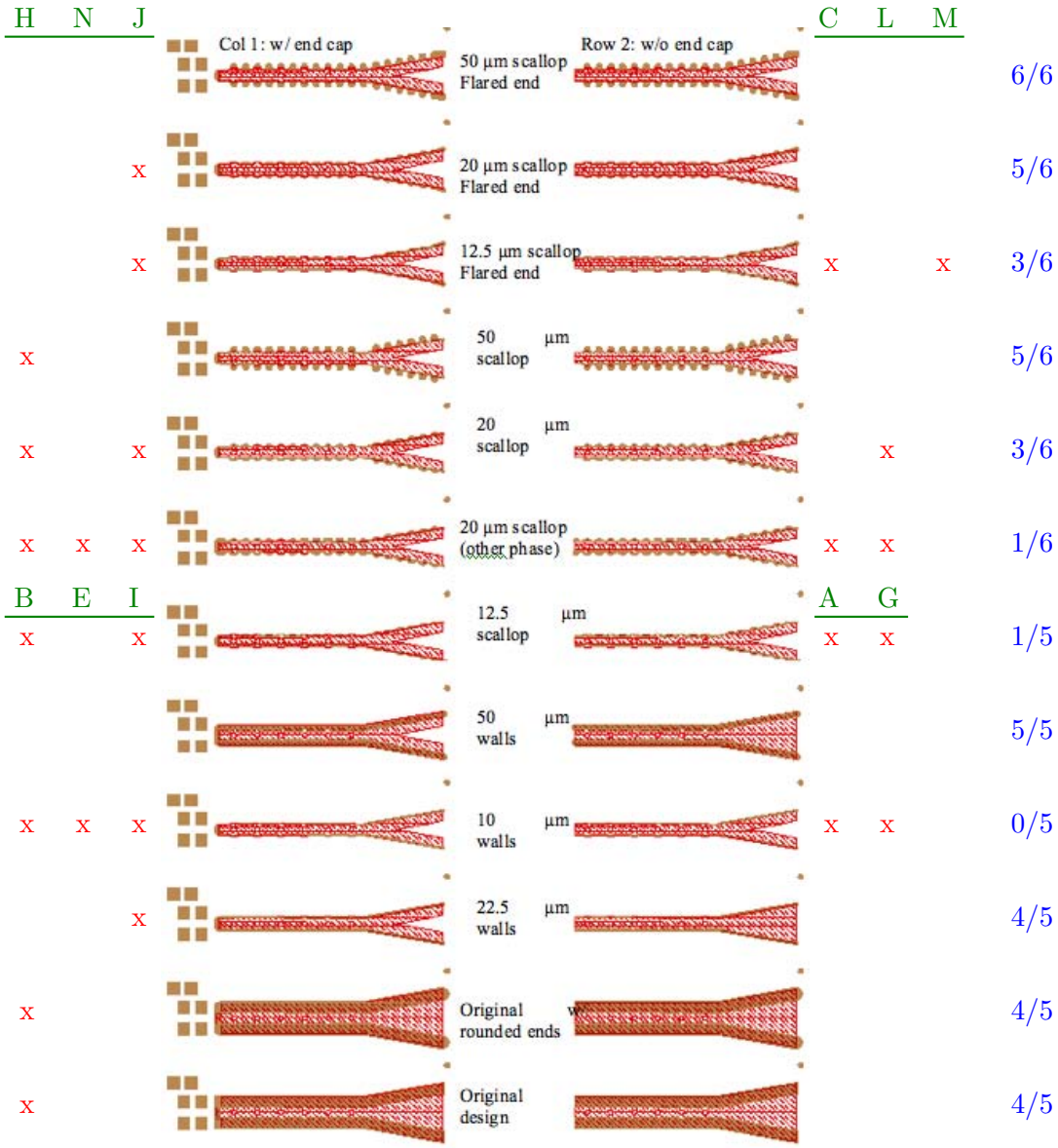

(b)

Figure 4.4. (a) Depiction of the wall shape of a scalloped waveguide. (b) Map of the waveguide geometries. The green letters denote the diced piece label, the red x's again denote the waveguides that cracked, and the blue ratios denote what fraction of the waveguides with a particular first level metal structure for the horn survived.

SEM Inspection of the cracking

We also examined samples A, B and C with SEM imaging. The purpose was to determine whether the SEM could find cracks that were not visible optically as well to confirm whether the apparent cracks observed optically were actually cracks under SEM inspection. This was useful in identifying many structures observed in the optical images which turned out not to be cracks.

Fig. 4.5 shows typical cracking seen near the ends of the 10 μm wide walled waveguides. In all cases the crack appears to start right at the tip of the metal wall.

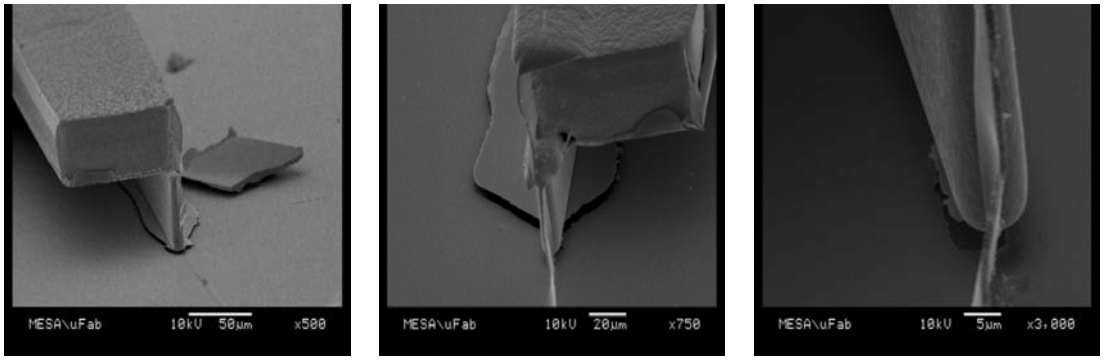

Figure 4.5. Three examples of cracks observed need the ends of horns with 10 micron wide walls: (a) Piece A , WG3 (b) Piece B, WG1, (c) Piece B, WG1 - opposite side.

As mentioned above the straight lines seen in the optical images of piece D are not actually cracks. Fig. 4.6 zooms in on a couple of these lines where we can see that these are thin lines of metal deposited on the surface. The lines are the result of cracking in the photoresist but not of the substrate. Both free space and integrated waveguides are fabricated with a thick, two-layer resist process. After the second layer lithography, the resist layers often form cracks originating at the corners of the waveguide walls. In many cases, this resist cracking allows solution migration down to the conductive substrate and results in Au electrofillng the bases of the cracks. The visible discolorations below are gold plating in the resist cracks.

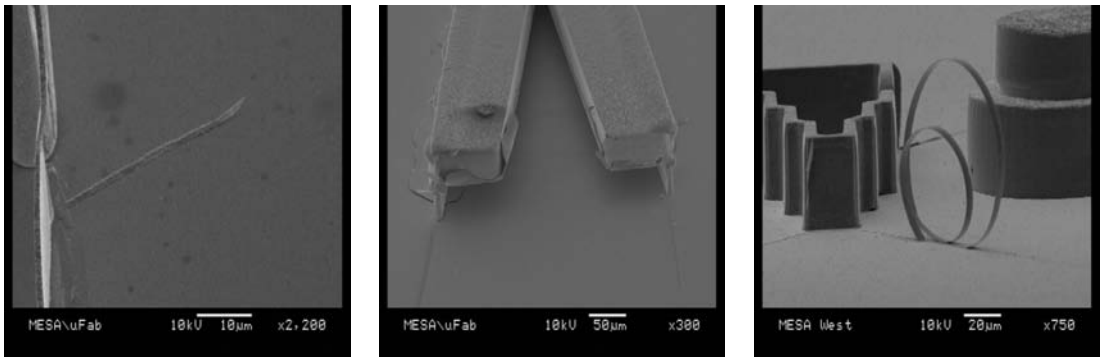

Figure 4.6. Three examples extra metal deposition that can appear to look like cracks in an optical microscope: (a) Piece A, WG1 (higher mag.), (b) Piece C, WG1, (c) Another wafer run, showing the metal peeling up.

In addition to the thin metal lines, we can also see a tall, approximately 1 μm wide, "sail" of metal in some of the images above (e.g. Figs. 4.5(b), 4.5(c), 4.6(a). This "sail" is more clearly seen in Fig. 4.7(a). This is also due to cracking in the photoresist, but the larger amount of plating suggests that a substatial gap opened up in the resist before or during plating. This is an issue since some of the these sails can end up in places that may effect the radiation properties of the horns (see Fig. 4.7(c)) or result in an electrical short as we will discuss below.

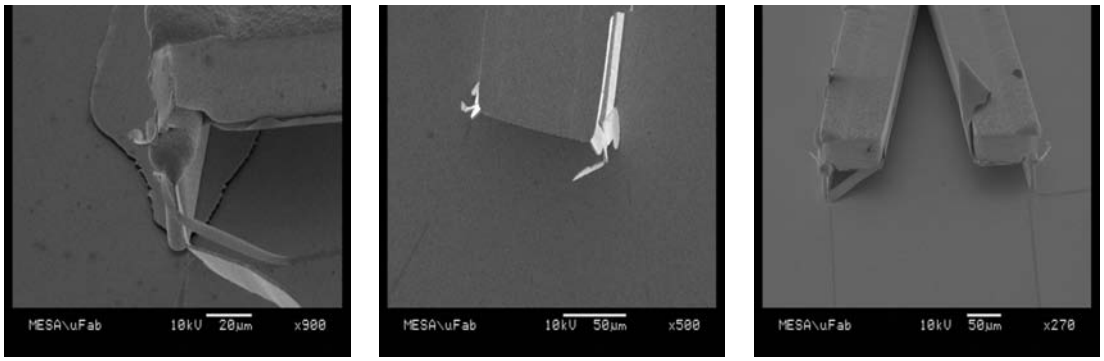

Figure 4.7. Three examples metal whiskers resulting from larger cracks in the photoresist: (a) Piece A , WG1 (b) Piece A, WG3, (c) Piece C, WG2.

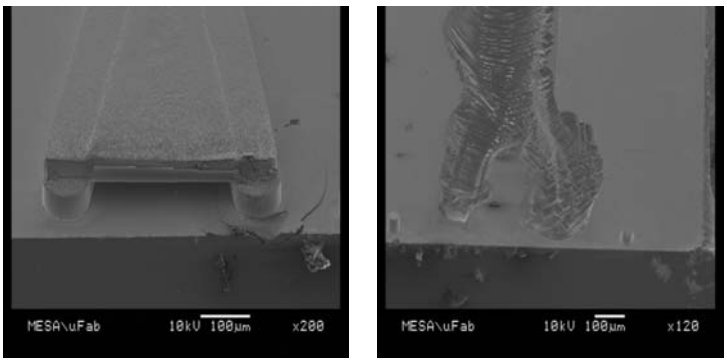

Figure 4.8. (a) The only 70 μm wide, rounded end, waveguide that cracked. It was also the only waveguide of theis type that terminated very near the cleave. (b) The neighboring waveguide with the same width but square corners completely delaminated.

Why do some of the cracks have a thin layer or metal and the others have a tall sail? A possible answer may be because this gold plating resulting from the resist cracking is likely poorly adhered to the substrate as the GaAs in this area still has a top Ti layer. Only the area under the gold walls was cleared of its top Ti layer to provide a pristine plating base. The poor adhesion between the plated gold in the resist cracks and the substrate would allow this metal to break off, leaving only the discolored lines extending out from the waveguides that optically look like cracks.

Another possible concern is that most of the waveguides tested in this experiment did not terminate near the edge of the chip. The one waveguide with 70 μm wide walls and rounded corners that did crack was piece B. This piece was one of the two that was cleaved such that the

waveguides were close to the edge (see Fig. 4.8(a)). One can see that the crack did not originate at the tip of the waveguide wall like the thin walled waveguides. Instead it appears to have started from a defect in the cleave. With the cleave close to the waveguide the GaAs may be weaker which would make it easier for the lateral stress from the waveguide length to crack the substrate. The cracks on the other two waveguides that cracked on this chip did not extend all the way to the facet as seen in Figs. 4.8(b) and 4.5(c), but both of these had sharp corners that could initiate cracking near their tips.

The waveguides with rounded ends having a radius of curvature larger than 10 μm, looked pretty good. Fig. 4.9 shows three of these waveguides. Not only are no cracks present in these examples, but it also appears that the resist does not crack for these waveguides. Therefore we do not see lines on the surface or sails that could be a problem.

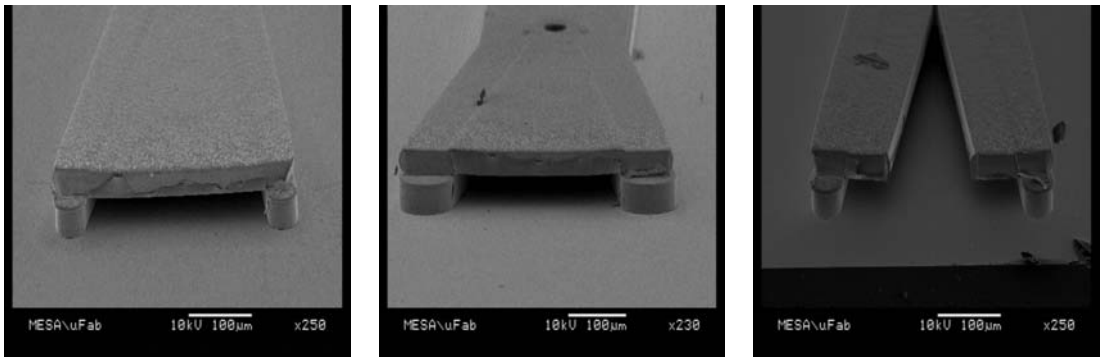

Figure 4.9. Three examples waveguides terminated in rounded ends displaying no whiskers or cracking: (a) Piece A , WG2 (b) Piece A, WG5, (c) Piece B, WG2.

Given these results, Mask Revision 6 changed the waveguides walls used with the lasers to be straight with wall thicknesses of 40 μm and rounded corners. Unfortunately, cracking still occurred around many of the waveguides, although few of the waveguides actually delaminated completely from the substrate.

4.2 Integrated Laser Performance

Given the complexity of the processing and the difficulty of making good metal-metal waveguided, THz QCLs in general, we were only able to make one functioning set of lasers during this project. These lasers were made from piece N of the MBE grown wafer VB0159. The resulting lasers, two of which are shown in Fig. 4.10, looked pretty good. However, the performance of the lasers was not as good as expected.

In a good THz QCL, the current should remain small until the applied voltage approaches the design bias, after which it should increase rapidly until the device hits a negative differential resistance (NDR) region. However, many of the lasers appeared to be short-circuited the first time they were measured. Plots of the voltage versus current (I-V) would show a linear relationship between the two parameters and resistances lower than 1 Ω. For most of these, if the current was

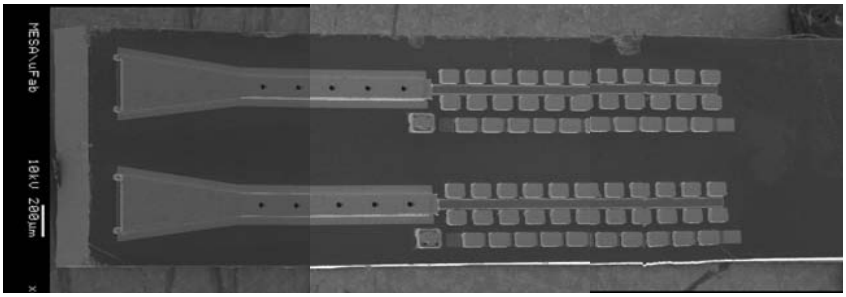

Figure 4.10. Composite SEM image of two QCLs integrated with rectangular waveguide horns before testing.

continually increased, instead of ever reaching an NDR the current would suddenly drop to a much lower value. This change was irreversible. Sometimes, there would be multiple irreversible changes. An example of this behavior is shown in Fig. 4.11 (USE IV of O4). The different colors in the plot correspond to sequential measurements of the I-V (starting from red and going to blue).

For some of these lasers, the I-V would eventually start to look like typical laser I-Vs. Fig. 4.12 shows the I-V for laser M4 before and after the irreversible change in the I-V. Before the snap, the initial IV not only started out too conductive but it started to curve the wrong direction. After the snap the curvature of the I-V switched to the correct sign, and NDR was observed (the kink near 0.1 A). More importantly, this sample lased as the current approached the NDR region.

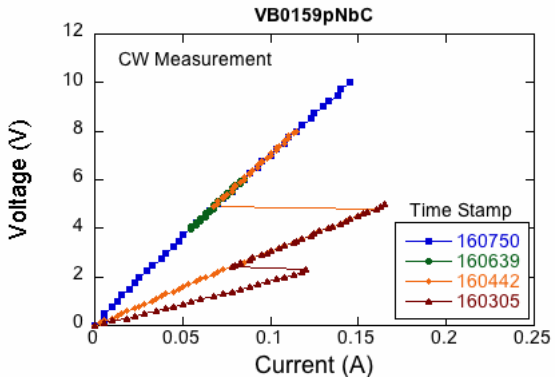

Figure 4.11. I-V for a QCL showing irreversible changes as the current increase enough to fuse metal whiskers on the chip. The colors correspond to the time sequence of the sequential measurements (red first to blue last.

The cause of the snapping I-V's is probably due to the metal whiskers that result from cracking of the resist mold during electroplating of the wvaeguides as discussed in section 4.1. An example of a whisker that is probably shorting a laser is shown in Fig. 4.13(b). In this image, a whisker is seen connecting a corner of the waveguide (which is connected to the laser ground) to one of the laser bias bond pads. Since the whiskers are very thin (on the order of a micron), they will act as fuses and melt once they begin to pass a high enough current. After which the current will again pass through the laser. While the whiskers are a nuisance, by themselves, they did not harm

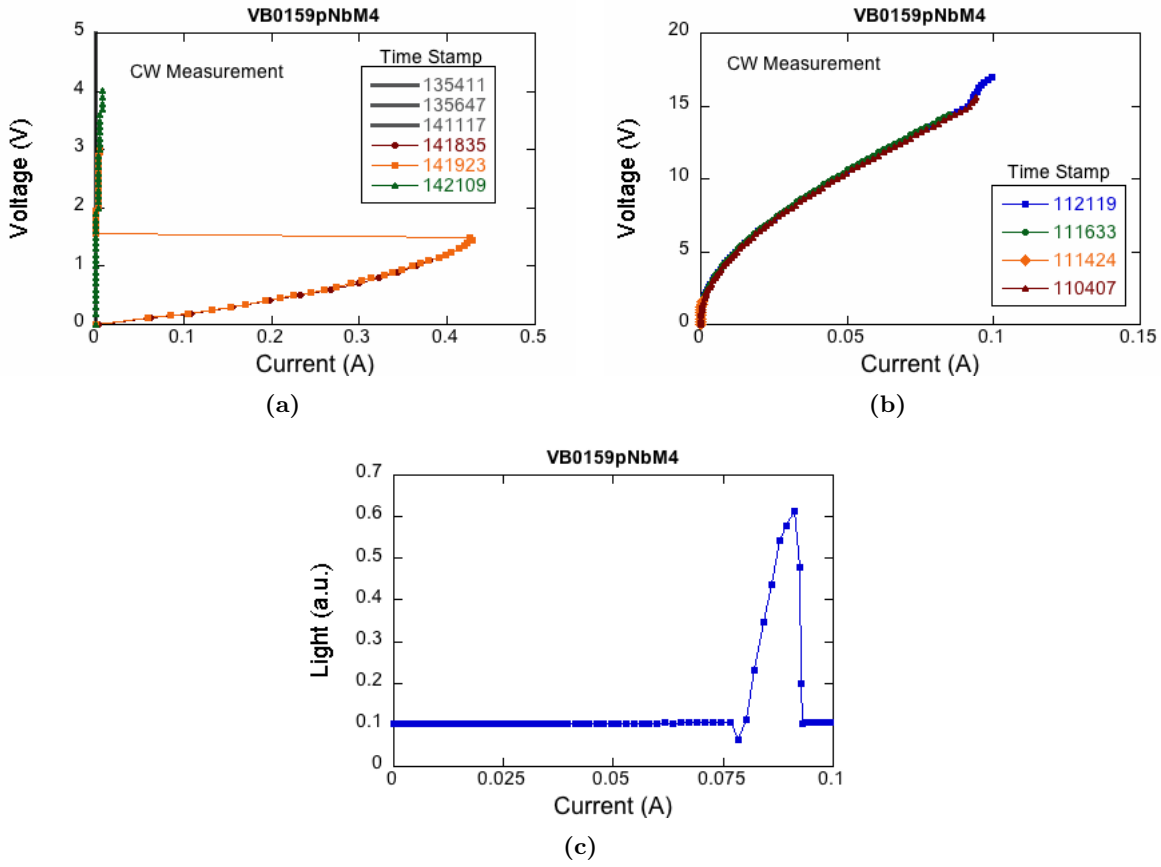

Figure 4.12. I-V for sample VB0159pNbM4 (a) before and (b) after the metal whisker fused. (c) Observation of lasing with a threshold of ≈ 0.075 A.

the laser performance. On one of the lasers the whisker never fused, but once the applied voltage reached the design bias the device still lased (it just had a large parallel current).

Unfortunately, the whiskers were not the biggest problem. The I-V in Fig. 4.12 shows that the voltage at which NDR occurs is near 15 V, and the voltage near threshold is near 12V. The design bias for this particular laser is 3 V and other of our lasers processed differently but with the same design for the active region work at this lower bias. Thus something is wrong with this device. The device still operates and lases at the design frequency so the MBE growth of the active layers must be correct. Since the device should only lase near the design bias, this implies that most of the voltage drop is not occurring in the active region. Thus there must be a large series resistance somewhere. Unfortuantely, we never figured out what the cause of this resistance was but it leads to two problems: excess heating and dielectric breakdown.

Excess heating of the laser will lower the output power and the maximum heat sink temperature at which the laser operates. In fact, the maximum heat sink temperature was 30K for these lasers. Given the facts that metal-metal waveguided THz QCLs typically have higher operating temperatures than plasmon waveguide QCLs, and the measured maximum temperature was more than a factor of two lower for typical lasers with this active region, it does appear that this extra resistance is heating the laser core.

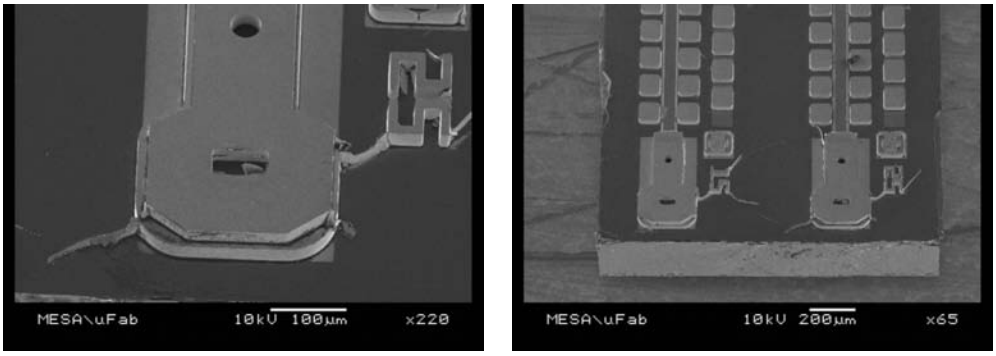

Figure 4.13. SEM image of lasers from sample VB0159pN. (a) shows a close-up showing some metal 'sails' coming from the corners resulting from cracked resist. (b) shows one of these 'sails' shoring the waveguide to the laser bias.

The bigger problem is that at high biases the devices themselves and not just the whiskers would fuse, thereby killing the device permanently. There is a very thin layer of SiN between the plated horn and the QCL embedded inside of it. From past experience we have noted that uniform layers of our SiN can demonstrate dielectric breakdown at threshold voltages as low as 25 volts. Our devices were tending to breakdown near 20 V. This may be because of the film quality, or it may have to do with the fact that our film covers non-planar surfaces, covers sharp corners and is sandwiched between GaAs and a big block of gold which we stated above has a significant thermal expansion mismatch. The exact location of the short in the device was not always visible but in many of the lasers, damage could be seen right at the horn laser interface as shown in Fig. 4.14.

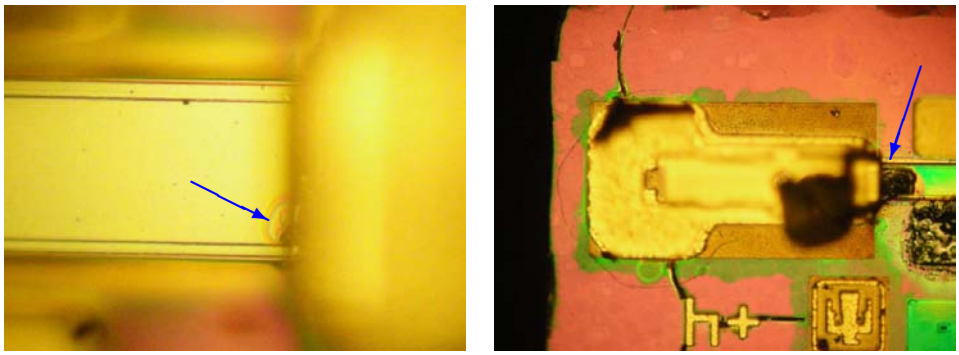

(a) **(b)**

Figure 4.14. Dielectric breakdown of the SiN at the laser / waveguide interface for two lasers. The image in (b) lead to a large enough current spike to melt the bondwire and pad at the edge of the image.

To check our hypothesis that the failure was indeed at this interface, we performed TIVA measurements on a few of the lasers. TIVA analysis for VB0159pNpI4 is shown in Fig. 4.15. Bright contrast in TIVA indicates a positive temperature coefficient (TC) (i.e. the resistance increases when exposed and heated by a thermal laser). In silicon devices, positive TC is normally seen

when there is a resistive short such as between metal and metal or between metal and heavily doped polysilicon . Dark contrast in the TIVA images indicates a negative TC (i.e. the resistance decrease when exposed to a thermal laser). Negative TC is normally observed when there is a short between metal and lightly doped silicon substrate in silicon devices. Many of the samples with a short show positive TC somewhere near the laser waveguide interface, indicating a resistive short there, although in some of the lasers other hot-spots were also observed. Therefore more work is still required to improve the laser / waveguide intergration.

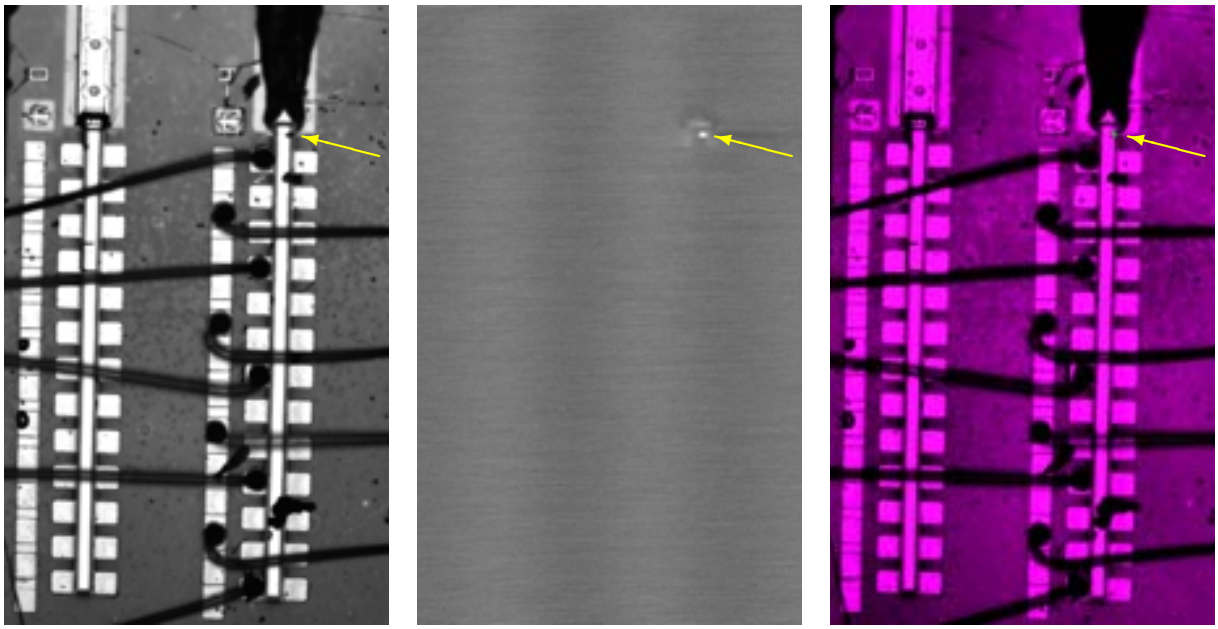

(a) (b) (c)

Figure 4.15. TIVA analysis which shows where the sample heats the most, and therefore by inference where the most current is flowing (indicated by the yellow arrows). (a) Reflected light image (b) TIVA image and (c) overlay of the two.

4.3 Measured QCL Beampatterns

The last issue we hoped to address during this project was measuring a beam pattern of radiation emitted by a QCL integrated directly into the rectangular waveguide on the same chip. At the end we only had time to measure the beampattern of one laser, and the maximum power that we were able to measure was only 1.8 μW. This value is significantly below our normal THz QCL lasers even with nominally identical active regions. We don't know if this is because of poor laser performance, poor waveguide performance or poor coupling between the laser and our measurement optics. Given the relatively low propagation loss observed in chapter 2, I suspect that the waveguides are not a problem.

Because most of our effort went into making the lasers, little time was left to measure the beampatterns. The measurement itself was very similar to the measurements of the stand-alone

waveguides as shown in Fig. 3.21. Again the lens was actually an off-axis parabolic mirror instead of a refractive lens. There were two main differences between the measurements. FIrst, the laser was integrated into the waveguide and second, there was a window between the waveguide and the OAP, since the device only operated at cryogenic temperatures. Both of these differences are important.

The fact that the laser is inside the waveguide means that it is much more difficult to align the collection optics. With the FIRL laser we aligned a HeNe laser to be collinear with the THz beam. Since the waveguides could be removed from the beam, we could use the visible HeNe to align the optics. Even with the waveguides in place, the HeNe propagated well enough through them to allow fine tuning of the alignment. This is not possible when the laser is in the waveguide.

The HDPE cryostat window was also opaque in the visible further preventing use of visible beams for alignment. We were unable to get a anti-reflection coated window for this effort which means that there was a high probability of multi-beam interference from reflections off of the window and the the laser mount. This should lead to similar interference patterns to those that we saw with in section 3.1.1. The window was also wedges at a 3° angle to minimize Fabry-Perot etalon effects, but we did not model the effect this would have on the beam.

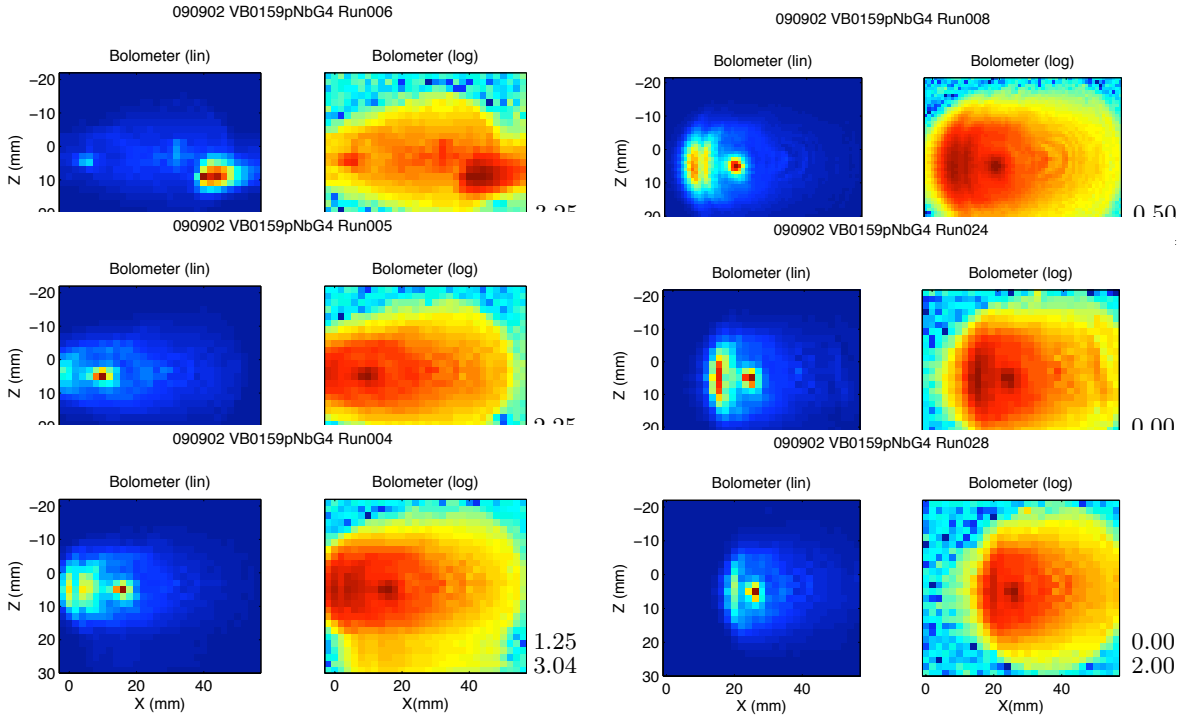

Figure 4.16. Measured beampattern image with different mirror positions. The vertical pair of numbers on the right of each image corresponds to the two micrometer readings.

Since we did not know the precise position for the mirror, we scanned the mirror position. The set of images in Fig. 4.16 show the measured beampatterns as the collection mirror was moved along both the X and Z axes (as defined in Fig. 3.24). It should be noted also that the waveguide for these measurements was rotated 90° compared to the stand-alone waveguide measurements due

to the cyrostat mounting requirements. Thus the beam center should be near the left edge of the mirror in the images.

The behavior of the resulting images as the mirror is translated agrees qualitatively with our expectation based on Fig. 3.25. The outline of the mirror appears to be most circular when the micrometer positions are (0.0, 2.0) and the effective size of this outline is roughly 50 x 50 mm in agreement with the actual mirror size. The beam does appear to be shifted to the left of center as expected given that these devices also have a finite substrate lip in front of the output aperture (see Fig. 4.10). What is not expected, however, is the shape of the beam. We did not expect either a nearly circular spot close to the center or the vertical line(s) closer to the mirror edge. If anything we expected horizontally orientated ellipse.

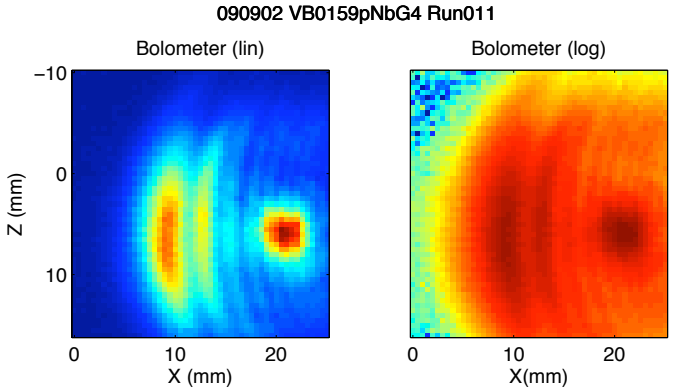

Figure 4.17. Higher-resolution image of the beampattern using a 1 mm diameter pinhole, showing interference effects.

As last look at the beam-pattern, fig 4.17 also shows a higher-resolution image for micrometer position (3.04, 0.5). Although not explored in depth, there again seems to be interference patterns showing up in the data. These patterns will have to be accounted for or removed before we can say conclusively what the true beampattern is.

Chapter 5

Conclusions

We were able to significantly improve the waveguide propagation loss measurements and now have confidence in the results. We believe that we measured the lowest waveguide loss in a THz rectangular waveguide ever reported - 1.3 dB / λ. Refining the process development boosted our confidence that all photoresist was removed from the waveguides, and using indium plated silicon strips removed the concern of indium pressing into the waveguides during mounting. We believe that we identified and removed all THz radiation leakage paths and that the measured transmission was accurate except when the signal on the bolometer was near the noise floor of the measurements. While we were able to measure the loss per length, we only had time to do so at a few different frequencies.

Future measurements could focus on more detailed exploration of the waveguides, including measurements at many more frequencies, trying to quantify the bend loss, and looking for the bandwidth reduction resulting from the release holes and their matching structures. Filling in the frequency gaps requires using lower power lines from a molecular gas laser, so higher throughput would be desired. Thus a new mask should be made that has waveguides shorter than 14 mm. With higher throughput, it would also be a good idea to add a spatial filter at the FIRL output to clean up the spatial mode at the input of the waveguides and further reduce feedback issues into the FIRL. In addition, since the real usefulness of these waveguides will come when integrated into more sophisticated circuits on chip, other functionalities could now be explored. These include some elements we already qualitatively demonstrated such as splitters, combiners and tees, in addition to higher functionality elements such as circulators to prevent feedback.

Our efforts on obtaining the far-field patterns is still incomplete both for the stand-alone and integrated waveguides. We were able to identify the source of interference in the stand-alone measurements and minimize them significantly. The interference in the integrated devices is probably of similar nature but was not conclusively shown. The biggest problem with the measurements to date is due to the lip in front of the waveguides causing the beam to steer away from the boresight of the waveguides and the large divergence angle expected due to the sub-wavelength aperture along one dimension. In the future, more sophisticated mounting options or a full half-paraboloidal mirror would significantly improve the measurements. If these improvements are eventually added, then we should explore the beam pattern dependence on the presence and shape of V-notches in the horns which are designed to narrow the divergence and lower the steering angles.

Finally, the integration of QCLs with integrated waveguides improved considerably. Cracking of the carrier substrate around the horns was significantly reduced. Further improvements are needed to reduce the number of whiskers resulting in electrical shorts. Also the interface between the laser and the horn should be re-examined to minimize the risk of dielectric breakdown, although this may be improved by finding the cause of the series resistance that forced higher voltage operation.

Appendix A

Processing Changes

A.1 Resist Thickness Uniformity Improvements

Techniques developed during the THz Grand Challenge resulted in successful fabrication of hollow, rectangular, 3-D, free space, waveguides. Some of these waveguides were designed with different lengths in an effort to extract the waveguide loss per length. These waveguides used the same horn on each waveguide to minimize differences in the coupling in and out from waveguide to waveguide. Another set of waveguides were designed with identical lengths of waveguides, but with different horns in an effort to determine if horns with slots could reduce diffraction in the vertical direction. To ensure that valid comparisons can be made between these different waveguides/horns we need to make sure that they are fabricated as designed.

Unfortunately, in some of the early runs, we found deviations of the waveguides from the desired shape. Figure A.1 has images captured with an optical microscope of waveguides when looked at end-on. While the waveguides shown should all be 37 μm tall, we can clearly see that the height of the waveguides are different, and that the lids are not completely parallel to the substrate. Since the frequency cutoff, dispersion, and coupling to free space will all depend of these variations in dimension we needed to eliminate these variations. Besides the waveguides being too tall, Fig. A.2 shows another issue - there is a gap between the lid and the sidewall. This can also increase the loss of the waveguide.

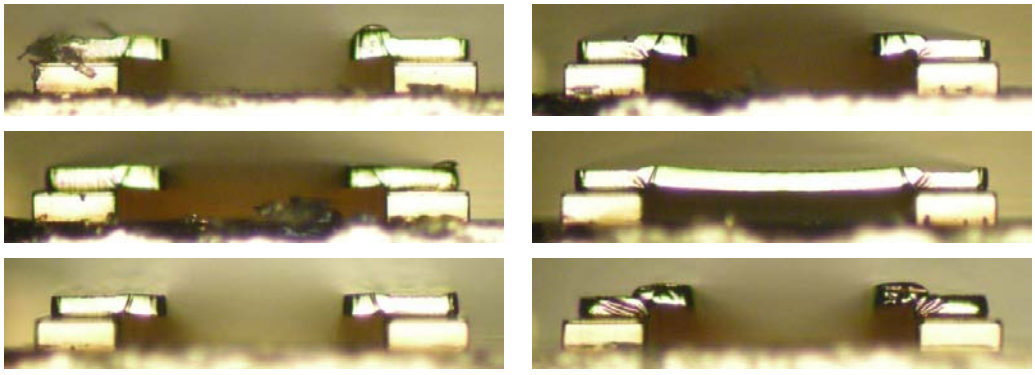

Figure A.1. Images of the ends of the waveguide openings of sample 06-24-08-02 row 5, taken end-on with an optical microscope. The images shown are of waveguides 1,3,5,7,9, and 11 on the chip.

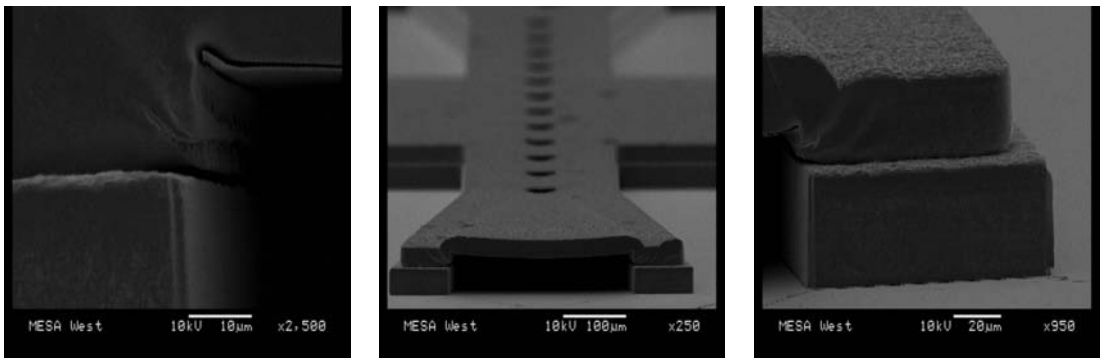

Figure A.2. SEM Images of the opening into a waveguide horn from sample 06-24-08-02, showing a gap between the lid and walls on the waveguide interior.

The waveguides are made in a two step lithographic process, but both the width and height of the waveguides are determined by the first layer of resist. The lateral openings in the the first resist layer define the location of the the sidewalls. After plating the sidewalls, this resist is left in place, to provide the base for plating the waveguide lids. Therefore, both uniformity in height and planarity of the first resist layer are essential.

The variations in the height of the waveguide lids were the result of photo resist non-uniformity during the lithography process. Typical photo resists are spin coated at 2K rpm or greater and have thickness deviations of ∼1-2% across the substrate. The photo resist used for this process was JSR Products NFR-015. This resist has similar thickness uniformity of ∼1-2% when processed at comparable spin speeds. However, to achieve the film thickness of 37 μm needed for the waveguide height, the NFR was processed at a much lower speed (475 rpm). This speed reduction was necessary to achieve the thickness needed over the majority of the substrate but was insufficient to ensure a uniform thickness over the entire area of a 4 wafer. In particular the edge bead was quite large and extended in a significant distance from the wafer edge. The resist height variation resulted in devices located towards the outer edges of the strips to be progressively taller than devices in the center of the strips.

While resist thickness variation can explain the taller waveguides than desired, it does not intuitively explain the gaps between the lid and the sidewalls. However, the higher resist is in fact the cause of this gap. The gold electroplating process used to deposit the walls and lids of the waveguides is specifically controlled to be level across the wafer and therefore was stopped once 37 μm of metal was deposited. This deposition was level with respect to the height of the resist mold in the center of the substrate but was ∼25% below the top of the resist mold along the perimeter affected by the thicker edge bead. The first layer of resist is covered by metal before spin coating the second resist. This taller, metal-covered resist, partially shadows the second layer resist, leading to incomplete development of the second resist layer. This thin remnant of resist leaves the gap seen once all the resist is removed after plating is complete.

To correct this problem, resists specifically designed for the thicknesses needed were considered, such as SU8. SU8 spin coated at ∼1000 rpm results in ∼30-40 μm thicknesses with a much smaller edge bead than NFR. In spite of this advantage, typical thicker, negative resists such as SU8 are notorious for the difficulty involved in completely removing the remaining polymer post processing.

This issue is more serious in processing 3D rectangular waveguides because the remaining resist is encapsulated inside of the waveguide making resist stripping even harder. Therefore, we decided to continue using NFR based because of its ability to be removed post processing.

To overcome NFRs non-uniformity issue, we explored different spin parameters : the substrate size, the resist temperature, and the spin speed. The actual parameters tested and the results of optical thickness measurements of as spun films are shown in table A.1. The best results were achieved by spinning 5 ml of NFR-015 onto a 5 inch wafer for 10 seconds at 550 rpm. The increase in wafer size did not improve the uniformity issue over the whole wafer. However, the edge bead was shifted out radially beyond the working 4 area where the devices were located. This provided improved local uniformity improvement in the area of interest to less than 1% in height variation. The edge bead results in imperfect mask contact, but this has not proved to be a serious issue.

Run	Wafer Size (in.)	Resist Temp (C)	Spin Speed (rpm)	Ave. Thickness (μm)	Std. Dev. (μm)
1	4	RT	450	46.07	19.63
2	4	14	450	48.14	13.64
3	4	14	1000	19.95	1.51
4	5	RT	450	43.77	0.50
5	5	14	450	43.15	0.56
6	5	-5	450	43.96	0.50
7	5	-5	1000	19.88	0.16
8	5	RT	500	42.86	0.58
9	5	RT	550	40.20	0.51
10	5	RT	600	36.27	0.53
11	6	RT	450	42.20	0.52

Table A.1. Parameters explored to find processing parameters to provide uniform, planar, 37 μm thick NFR films.The average thickness and stardard deviation were only recorded over the central 4" diameter area of the wafer.

The thickness of the film spun at 550 rpm, measured optically before the film was processed with a KV-300, was a little over 40 microns. This is thicker than the desired 37 μm, but, after further processing (exposing the film, and developing the pattern - see Fig. A.3), the average film thickness measured by Dektak was only 37.4 μm (see Table A.2). It is unknown whether the height discrepancy is the results of further processing or calibration errors between the two measurement techniques. In either case, the thickness is reproducible allowing us to create the correct thickness. The uniformity can also be seen in the SEMs of the final waveguides shown in Fig. A.4.

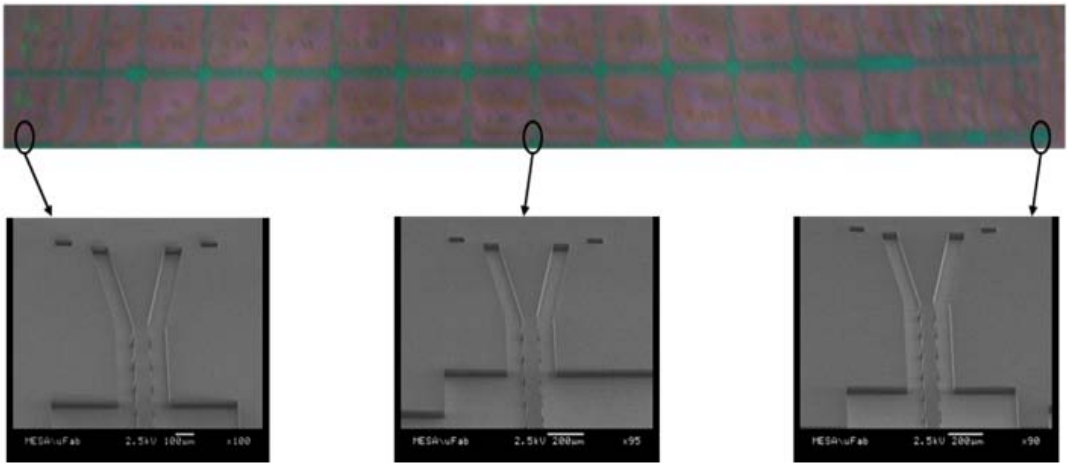

Figure A.3. Optical image of the first layer resist defining the waveguide wall, and SEM images at 3 locations. The thickness of the resist measured by the Dektak for all of the waveguides on the strip are given in table A.2. The thickness measurement was made on both sides of the waveguides.

Horn	Left Depth (μm)	Right Depth (μm)
1	36.95	37.15
2	37.19	37.18
3	37.27	37.38
4	37.62	37.33
5	37.43	37.53
6	37.36	37.11
7	37.39	37.12
8	37.45	37.25
9	37.65	37.46

Horn	Left Depth (μm)	Right Depth (μm)
10	37.71	37.61
11	37.53	37.56
12	37.55	37.19
13	37.46	37.39
14	37.56	37.48
15	37.48	37.57
16	37.22	37.25
Ave.	**37.43**	**37.35**
Std. Dev.	**0.2**	**0.17**

Table A.2. Variation in the measured depth of the NFR-015 resist of 16 waveguides. The measurement was made after resist development but before plating.

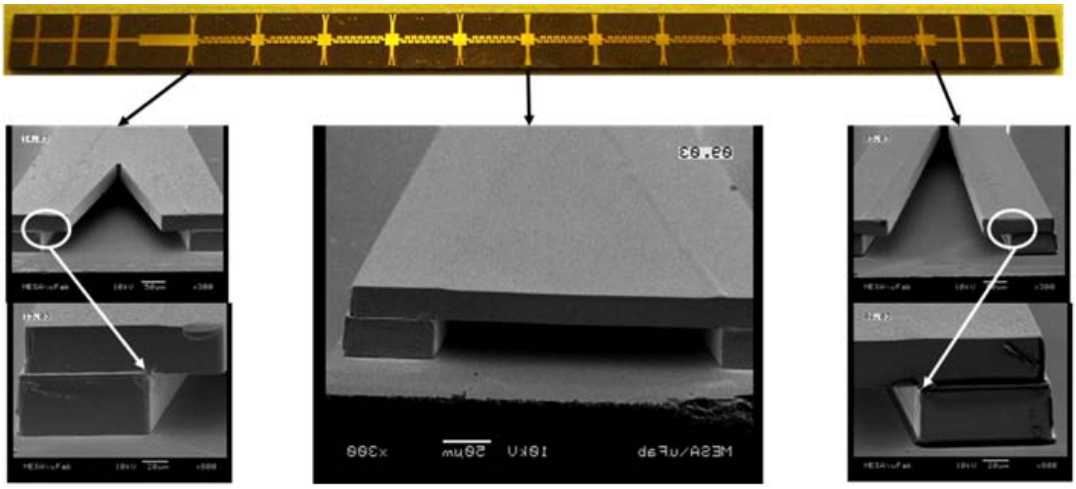

Figure A.4. Optical image of a row of waveguides and SEM of the waveguide openings at thre different positions along the chip. The height of the waveguides is uniform and the gaps seen previously between the walls and the lids is gone.

Possible Future Improvements

Although using a two layer plating process works, there would still be significant advantage to developing a single plating layer process. In addition to removing a time consuming plating step, this would eliminate the need to align the lids to the waveguide walls. In addition there would be no worries about the a resist foot causing a gap between the metal layer interface in the inside of the waveguide (at least not between the lid and the walls). The way we removed the resist foot in the existing two layer process was to monitor the plating rate very carefully and stop the plating right as soon as it was as tall as the resist. A single layer plating step would remove this requirement making the process much easier and eliminate potential errors such as when a power supply fails and provides too much current as shown in Fig. A.5. We did try a single layer process once under the grand challenge, but there appeared to be a plating gap at the interface of the walls and the substrate. It is possible that this gap was also due to a resist foot.

Another issue that needs to be addressed is the removal of the seed layer from the release holes and the ends of the horns. The layer is thick enough that it does not always break away during development as shown in Figs. A.6 and A.5(a,b). This has two possible impacts. First, if the metal layer doesnt break out this can significantly slow the development time of the waveguides by preventing developer from getting in to the waveguide. Second, if the metal tabs are still present they could fall into the waveguide which would effect propagation or remain on the horn edges which would effect the radiation patterns of the horns. The titanium layer is probably etched off by the HF dip, but the gold layer can not easily be removed. A wet etch will eat part of the waveguide, while ion milling the layer partway through the resist removal would effective harden the resist both due to the time and due to solvent outgassing in the vacuum.

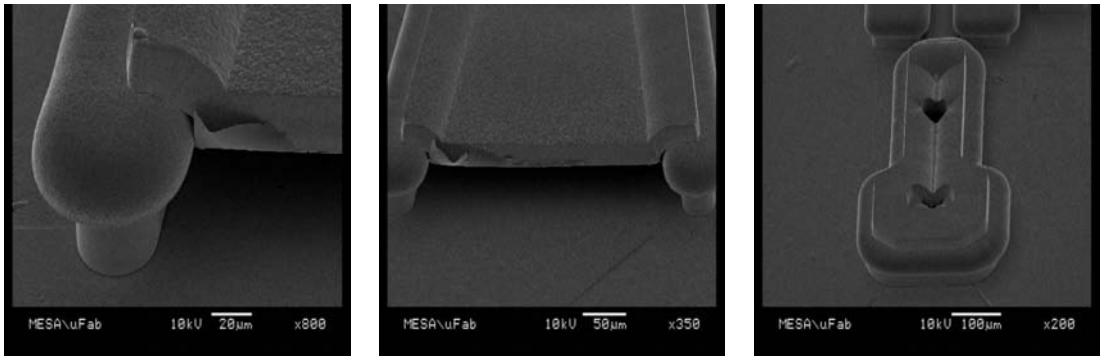

Figure A.5. SEM Images of the resulting waveguides when the plating power supply failed causing the current set point to double and the plating thickness to overshoot by roughly 20 μm on sample VB0232I. In (a) and (b) we can see that a gap formed between the lid and the overplated sidewall which will impact the waveguide propagation and in (c we can see that the vertical emission port has been shrunk.

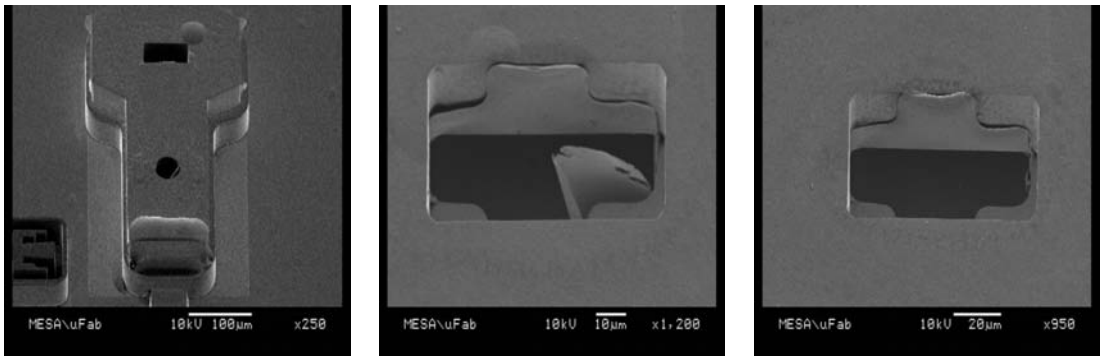

Figure A.6. SEM images showing that the seed layer is not breaking out completely and is remaining in the release holes as well as the vertical emission holes.

A.2 Mask Revisions

The basic mask sets used in this project were created in the THz microelectronic Transceiver Grand Challenge LDRD. For documentation of this mask set refer to SAND2008-7337.

Mask Revision 5: Reduce number of variations on maskset

This revision was intended to reduce the amount of variation relative to the previous versions of the maskset. In many cases, the waveguides with multiple corners and different lengths confounded the results of the QCL measurement, so it was desired to make a new layout with identical horns on each laser.

The active region layout for revision 5 is shown in Figure 5. The bottom half of the layout

includes the standard laser design and interface (with a 65 μm wide laser bar protruding 5 μm into the waveguide), while the top half includes experiments on the laser offset and tapered transition.

The bottom four rows of the offset/taper experiment array are the offset experiment. Starting at the bottom row the offsets from the nominal design are -4, 0, +4, and +8. The top four rows of the array are the taper designs, with taper values of 45 μm, 35 μm, 25 μm, and 15 μm (from top to bottom). All of the lasers are labeled with either the offset or the taper.

Eliminating the corner sections from the output of the lasers also eliminated the dicing difficulty that was observed during previous versions of this maskset.

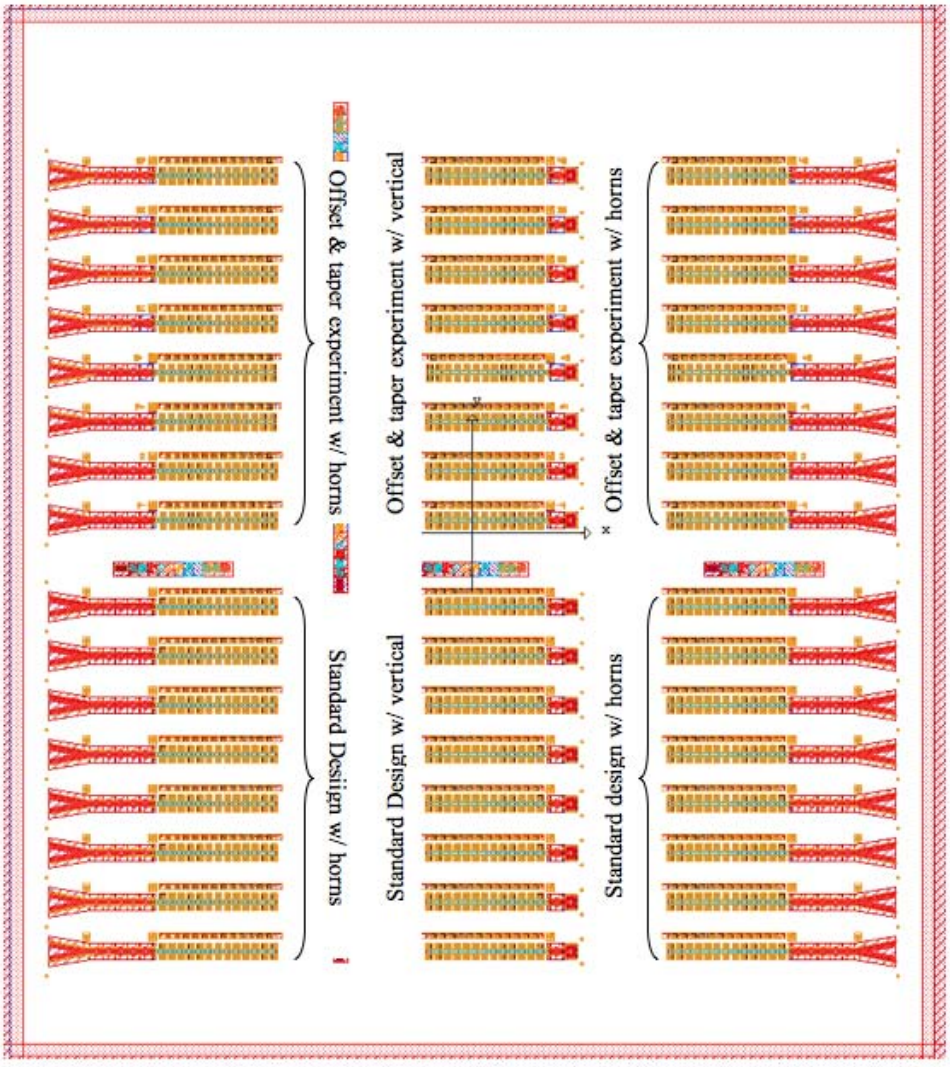

Figure A.7. Mask layout for intergrated waveguides starting with revision 5.

Mask Revision 6: Single straight-walled waveguides

Revision 6 is similar to revision 5, except that the waveguide walls in the active QCL region are all 40 μm wide. This thickness appeared to give the least cracking when test samples were cooled down.

The areas outside of the QCL regions are identical to revision 5, as are the experiments within the QCL region.

Only the two electroplating layers were revised and ordered. All other layers match to rev5.

DISTRIBUTION:

2	MS 1082	Mike Wanke, 1725
1	MS 1423	Greg Hebner, 1128
1	MS 1421	Jerry Simmons, 1120
1	MS 1071	Andy Boye, 1720 (electronic copy)
1	MS 1086	Dan Barton, 1123 (electronic copy)
1	MS 1315	Mark Lee, 1123 (electronic copy)
1	MS 1085	Chris Nordquist, 1742 (electronic copy)
1	MS 1085	Mike Cich, 1742 (electronic copy)
1	MS 1082	Adam Rowen, 1725 (electronic copy)
1	MS 1082	Christian Arrington, 1725 (electronic copy)
1	MS 1082	Chuck Fuller, 1725 (electronic copy)
1	MS 1082	Albert Grine, 1725 (electronic copy)
1	MS 1082	Rusty Gillen, 1725 (electronic copy)
1	MS 0899	Technical Library, 9536 (electronic copy)
1	MS 0161	Patent and Licensing Office, 11500 (electronic copy)
1	MS 0123	D.L. Chavez, LDRD Office, 1011 (electronic copy)


Sandia National Laboratories